

27 **Abstract**

28 A fundamental challenge in cognitive neuroscience is to develop
29 theoretical frameworks that effectively span the gap between brain and behavior,
30 between neuroscience and psychology. Here, we attempt to bridge this divide by
31 formalizing an integrative cognitive neuroscience approach using dynamic field
32 theory (DFT). We begin by providing an overview of how DFT seeks to understand
33 the neural population dynamics that underlie cognitive processes through previous
34 applications and comparisons to other modeling approaches. We then use
35 previously published behavioral and neural data from a response selection
36 Go/Nogo task as a case study for model simulations. Results from this study
37 served as the 'standard' for comparisons with a model-based fMRI approach using
38 dynamic neural fields (DNF). The tutorial explains the rationale and hypotheses
39 involved in the process of creating the DNF architecture and fitting model
40 parameters. Two DNF models, with similar structure and parameter sets, are then
41 compared. Both models effectively simulated reaction times from the task as we
42 varied the number of stimulus-response mappings and the proportion of Go trials.
43 Next, we directly simulated hemodynamic predictions from the neural activation
44 patterns from each model. These predictions were tested using general linear
45 models (GLMs). Results showed that the DNF model that was created by tuning
46 parameters to capture simultaneously trends in neural activation and behavioral
47 data quantitatively outperformed a Standard GLM analysis of the same dataset.
48 Further, by using the GLM results to assign functional roles to particular clusters
49 in the brain, we illustrate how DNF models shed new light on the neural
50 populations' dynamics within particular brain regions. Thus, the present study
51 illustrates how an interactive cognitive neuroscience model can be used in practice
52 to bridge the gap between brain and behavior.

53 **1. Introduction**

54 Although great strides have been made in understanding the brain using data-
55 driven methods (Smith et al., 2009) to understand the brain's complexity, human
56 neuroscience will need sophisticated theories (Gerstner, Sprekeler, & Deco, 2012). *But*
57 *what would a good theory of brain function look like?* Addressing this question requires
58 theories that bridge the disparate scientific languages of neuroscience and psychology.

59 Turner et al. (2016) described three categories of approaches to this issue using
60 model-based cognitive neuroscience that bridge the gap between brain and behavior by
61 bringing together fMRI data and cognitive models (Turner, Forstmann, Love, Palmeri, &
62 Van Maanen, 2016). The first approach uses neural data to guide and inform a behavioral
63 model, that is, a model that mimics features of responses such as reaction times and
64 accuracy. One example of this approach is the Leaky Competing Accumulator model by
65 Usher and McClelland (Usher & McClelland, 2001). This is a mechanistic model for
66 evidence accumulation, which incorporates well-known properties of neuronal ensembles
67 such as leakage and lateral inhibition. The model provides a good fit for a range of
68 behavioral data, for example, time-accuracy curves and the effects of the number of
69 alternatives on choice response times. Unfortunately, as remarked by Turner et al., this
70 mechanistic approach stops short of establishing any direct connection to the dynamics
71 of particular neural circuits or brain areas.

72 The second type of approach uses a behavioral model and applies it to the
73 prediction of neural data. One example of this approach is Rescorla and Wagner's (1972)
74 model of learning conditioned responses. In this model, the value of a conditioned
75 stimulus is updated over successive trials according to a learning rate parameter. The
76 model produces trial-by-trial estimates of the error between the conditioned and
77 unconditioned stimuli. This measure can then be used in general linear models to detect
78 patterns matching the model predictions within fMRI data. The method potentially allows
79 one to identify neural processes that are not directly measureable through behavioral
80 results (Davis, Love, & Preston, 2012; Mack, Preston, & Love, 2013; Palmeri, Schall, &
81 Logan, 2015). However, a drawback of this model-based fMRI approach is that it does

82 not explain cognitive states encoded by patterns of activation distributed over multiple
83 voxels in the brain.

84 The last, and most difficult approach is an *integrative* cognitive neuroscience
85 approach where a model simultaneously predicts behavioral and neural data. That is, the
86 model explains what the brain is doing in real-time to generate specific patterns of fMRI
87 *and* behavioral data. Turner et al. acknowledge that there are relatively few examples in
88 this category. For instance, they highlight recent papers that use cognitive architectures
89 such as ACT-R ('Adaptive Control of Thought – Rational') to capture simultaneously fMRI
90 and behavioral data (Anderson, Matessa, & Lebiere, 1997; Borst & Anderson, 2013;
91 Borst, Nijboer, Taatgen, Van Rijn, & Anderson, 2015). Although we agree that this
92 approach has immense potential, this is a relatively limited example of an integrative
93 cognitive neuroscience approach because ACT-R is not a neural process model. Thus,
94 ACT-R does not capitalize on constraints regarding how real brains actually work.

95 An alternative approach that does capitalize on neural constraints was proposed
96 by Deco et al (Deco, Rolls, & Horwitz, 2004). These researchers used integrate-and-fire
97 attractor networks to simulate neural activity from a 'where-and-what' task. The model
98 includes several populations of simulated neurons to reflect networks tuned to specific
99 objects, positions, or combinations thereof. The authors then define a local field potential
100 (LFP) measure from each neural population by averaging the synaptic flow at each time
101 step. To generate a BOLD response, they convolved the LFP measure with an impulse
102 response function. Although one version of the model was able to approximate single
103 neuron recordings from a prior study, as well as a measured fMRI pattern in dorsolateral
104 prefrontal cortex, other fMRI patterns from the ventrolateral prefrontal cortex were not
105 modeled. Moreover, comparisons to fMRI data were made qualitatively via visual
106 inspection. No attempt was made to quantitatively relate the measures. Finally,
107 behavioral data from this study were not a central focus. Such issues are relatively
108 common when modeling relies on biophysical neural networks due to the immense
109 computational challenges of simulating such networks. Appropriate partitioning of the
110 parameter space and estimation of model parameters are, in general, difficult steps of

111 this approach (see Anderson, 2012; Turner et al., 2016).

112 Inspired by this work, Buss, Wifall, Hazeltine, and Spencer (2014) adapted this
113 approach to simultaneously model behavioral and fMRI data from a dual-task paradigm
114 (Buss, Wifall, Hazeltine, & Spencer, 2013). They first constructed a dynamic neural field
115 (DNF) model of the dual-task paradigm reported by Dux and colleagues (Dux et al., 2009).
116 The model quantitatively fit a complex pattern of reaction time changes over learning,
117 including the reduction of dual-task costs over learning to single task levels. These
118 researchers then generated a LFP measure from each component of the neural model
119 and convolved the LFPs with an impulse response function to generate BOLD responses
120 from the model. The DNF model captured key fMRI results from Dux et al., including the
121 reduction of the amplitude of the hemodynamic response in inferior frontal junction in
122 dual-task conditions over learning. Moreover, Buss et al. contrasted competing
123 predictions of the DNF model and ACT-R, showing that changes in hemodynamics over
124 learning predicted by the DNF model matched fMRI results from Dux et al., while
125 predictions from ACT-R did not.

126 It is important to highlight several key points achieved by Buss et al. (2013). First,
127 the DNF model simulated neural dynamics in real time. The dynamics created robust
128 'peaks' of activation that were directly linked to behavioral responses by the model, and
129 these responses quantitatively captured a complex pattern of reaction times over
130 learning. Second, the same neural dynamics that quantitatively fit behavior also simulated
131 observed hemodynamics measured with fMRI. Finally, Buss et al. demonstrated the
132 specificity of these findings by contrasted predictions of two theories. Thus, their work
133 constitutes a notable example of an integrative cognitive neuroscience approach using a
134 neural process model that capitalizes on constraints regarding how brains work.

135 The current paper builds on the above example, by formalizing an integrative
136 cognitive neuroscience approach using dynamic neural fields. Our paper is tutorial in
137 nature, walking the reader through each step of this model-based cognitive neuroscience
138 framework. We extend the work of Buss et al. (2013) by (1) formalizing several steps
139 regarding the calculation of LFPs from dynamic neural fields and the generation of BOLD

140 predictions; (2) adding new methods to quantitatively evaluate BOLD predictions from
141 dynamic neural field models using general linear models (GLM), inspired by other model-
142 based fMRI approaches; and (3) adding new methods to identify model-based functional
143 networks from group-level GLM results. These methods allow for effectively identifying
144 where particular neural patterns live in the brain, as well as specifying their functional
145 roles.

146 The paper proceeds as follows. We begin with a brief introduction to dynamic field
147 theory. This places our model-based approach within a broader context for readers who
148 might be less familiar with this theoretical approach. Next, we introduce the particular
149 case study we will use throughout the paper, that is, the particular behavioral and fMRI
150 data set that serves as the basis for the tutorial. We then discuss the DNF model that we
151 used to capture simultaneously behavioral and neural data from this study, explaining
152 where this model comes from and how we approached the simulation case study. The
153 presentation will highlight key issues that theoreticians face when adopting an integrative
154 cognitive neuroscience approach. Next, we present behavioral fits of the data and discuss
155 strengths and limitations of the DNF model at this level of analysis.

156 After considering the behavioral data, we introduce a step-by-step guide to
157 generating hemodynamic predictions from dynamic neural field models. We then discuss
158 how to evaluate these predictions using general linear modeling (GLM). We first evaluate
159 the model predictions at the individual level. We then move to the group level, showing
160 how our approach can be used to identify model-based functional networks. To evaluate
161 these networks, we compare our approach to standard fMRI analyses, highlighting
162 examples where the DNF model sheds interesting light on the functional roles of particular
163 brain regions. The tutorial concludes with a general evaluation of our model-based
164 approach, highlighting strengths, weaknesses, and future directions.

165

166 **2. Overview of Dynamic Field Theory**

167 The present report introduces a tutorial on an integrative model-based fMRI
168 approach using Dynamic Field Theory (DFT). Thus, for clarity, before explaining the

169 integrative cognitive neuroscience approach, we start by giving a brief introduction to
170 DFT. Readers are referred to the DFT Research Group (2015) for a thorough treatment
171 of these ideas.

172 DFT grew out of the principles and concepts of dynamical systems (Gregor
173 Schöner et al., 2015) theory initially explored in the ‘motor approach’ pioneered by Gregor
174 Schöner, Esther Thelen, Scott Kelso, and Michael Turvey (Kelso, Scholz, & Schöner,
175 1988; Schöner & Kelso, 1988; Turvey, 1995). The goal was to develop a formal, neurally-
176 grounded theory that could bring the concepts of dynamical systems theory to bear on
177 issues in cognition and cognitive development (for discussion, see Spencer & Schöner,
178 2003). DFT was initially applied to issues closely aligned with the cognitive aspects of
179 motor systems such as motor planning for arm and eye movements (Erlhagen & Schöner,
180 2002; Kopecz & Schöner, 1995). Subsequent work extended DFT, capturing a wide array
181 of phenomena in the area of spatially-grounded cognition, from infant perseverative
182 reaching (Smith, Thelen, Titzer, & McLin, 1999; Thelen, Schöner, Scheier, & Smith, 2001)
183 to spatial category biases to changes in the metric precision of spatial working memory
184 from childhood to adulthood (Schutte, Spencer, & Schöner, 2003; Simmering, Peterson,
185 Darling, & Spencer, 2008). In the last decade, DFT has been extended into a host of other
186 domains including visual working memory [VWM] (Johnson, Hollingworth, & Luck, 2008;
187 Johnson, Spencer, Luck, & Schöner, 2009; Schneegans, Spencer, Schöner, Hwang, &
188 Hollingworth, 2014), retinal remapping (Schneegans & Schöner, 2012), preferential
189 looking and visual habituation (Perone, Spencer, & Schöner, 2007; Perone & Spencer,
190 2008), spatial language (Lipinski, Spencer, & Samuelson, 2010), word learning
191 (Samuelson, Jenkins, & Spencer, 2015), executive function (Buss & Spencer, 2008), and
192 autonomous behavioral organization in cognitive robotics (Sandamirskaya & Schöner,
193 2010).

194 The dynamic field framework was initially developed to understand brain function
195 at the level of neural population dynamics. Evidence suggests that local neural
196 populations move into and out of attractor states, reliable patterns of activation that the
197 neural population maintains in the context of particular inputs. For instance, when

198 presented with visual input, neural populations in visual cortex create stable ‘peaks’ of
199 activation that indicate that something is on the left side of the retina (Erlhagen, Bastian,
200 Jancke, Riehle, & Schöner, 1999; Markounikau & Jancke, 2008). These local decisions—
201 peaks—then share activation with other neural populations—other peaks—creating a
202 macro-scale brain state. Thinking, according to DFT, is the movement into and out of
203 these states. Behaving is the connection of these states to sensorimotor systems.
204 Learning is the refinement of these patterns via the construction of localized memory
205 traces and connectivity between fields. Development is the shaping of neural activation
206 patterns step-by-step through hours, days, weeks, and years of generalized experience.

207 Formally, dynamic neural field models are in a class of bi-stable neural networks
208 first developed by Amari (Amari, 1977), and then studied theoretically and
209 computationally by many research groups over last two decades (Bressloff, 2001;
210 Coombes & Owen, 2005; Curtu & Ermentrout, 2001; Ermentrout & Kleinfeld, 2001; Jirsa
211 & Haken, 1997; Laing & Chow, 2001; Wilson & Cowan, 1973; Wong & Wang, 2006).
212 Activation in these networks--called 'cortical fields'--is distributed over continuous
213 dimensions—space, movement direction, color, and so on. Importantly, patterns of
214 activation can live in different “attractor” states: a resting state; an input-driven state where
215 input forms stabilized “peaks” of activation within a cortical field, but peaks go away when
216 input is removed; and a self-sustaining or working memory state where activation peaks
217 remain stable even in the absence of input. Movement into and out of these states is
218 assembled in real-time depending on a variety of factors including inputs to a field.
219 Critically, though, activation patterns can “rise above” the current input pattern via
220 recurrent interactions: activation can be in a stable “on” state where subsequent inputs
221 are suppressed. That said, the “on” state is still open to change: in the presence of
222 continued input, the network might “update” its decision to focus on one item over another.
223 This points toward flexibility—how activation patterns can go smoothly and autonomously
224 from one stable state to another.

225 To date, several strengths of DFT are evident. First, DFT provides a *predictive*
226 language to understand both brain and behavior. DFT has been used to test specific

227 predictions about early visual processing, attention, working memory, response selection,
228 and spatial cognition at behavioral and brain levels using multiple neuroscience
229 technologies (Johnson, Spencer, Luck, & Schöner, 2009; Valentin Markounikau, Igel,
230 Grinvald, & Jancke, 2010; Schneegans et al., 2014; Schutte et al., 2003). Second, DFT
231 scales up. Across several papers, we have demonstrated, for instance, that ‘local’
232 theories of attention, working memory, and response selection can be integrated in a
233 large-scale neural model that explains and predicts how humans represent objects in a
234 visual scene - see Schöner, Spencer & the DFT Research Group, 2015. Third, DFT is
235 well positioned to bridge the gap between brain and behavior, simultaneously generating
236 real-time neural population dynamics and responses that mimic behavior, often in
237 quantitative detail (Buss et al., 2013; Erlhagen & Schöner, 2002).

238 The neural grounding of DFT has been investigated using both multi-unit neurophysiology
239 (Bastian, Riehle, Erlhagen, & Schöner, 1998; Erlhagen et al., 1999) and voltage-sensitive
240 dye imaging (Markounikau, Igel, Grinvald, & Jancke, 2010). Data from these studies
241 demonstrate that DFT can capture the details of neural population activation in the brain
242 and generate novel, neural predictions (Bastian, Schöner, & Riehle, 2003; Markounikau
243 et al., 2010). Thus, the neural grounding of DFT extends beyond mere analogy. Rather,
244 DFT implements a set of formal hypotheses about how the brain works that can be directly
245 tested using neuroscience methods. It was the success of this framework at capturing the
246 details of neural population dynamics in the brain that encouraged us to consider the
247 mapping between neural population dynamics and the BOLD signal measured with fMRI.
248 The integrative cognitive neuroscience approach detailed here is a critical step in this new
249 direction.

250

251 **3. Introduction to the case study**

252 To illustrate the model-based approach to fMRI using DFT, we have to select a
253 specific case study. This anchors the modeling approach to a specific task, a specific set
254 of behaviors, and a specific fMRI data set. Here, we use as case study the neural and
255 behavioral dynamics that underlie response selection. Response selection has been

256 studied using DFT for almost two decades at both behavioral (Christopoulos, Bonaiuto,
257 & Andersen, 2015; Erlhagen & Schöner, 2002; Klaes, Schneegans, Schöner, & Gail,
258 2012; McDowell, Jeka, Schöner, & Hatfield, 1998, 2002; Schutte & Spencer, 2007) and
259 neural levels (Bastian et al., 1998; Erlhagen et al., 1999; McDowell et al., 2002). Thus,
260 there is a rich history to build on. Furthermore, the last decade has seen an explosion of
261 research examining the behavioral and neural bases for response selection and inhibition
262 using fMRI. This stems, in part, from the clinical relevance of this topic: poor performance
263 on response selection tasks has been linked to performance deficits in atypical
264 populations (Kaladjian et al., 2011; Monterosso et al., 2005; Pliszka, Liotti & Woldorff,
265 2000).

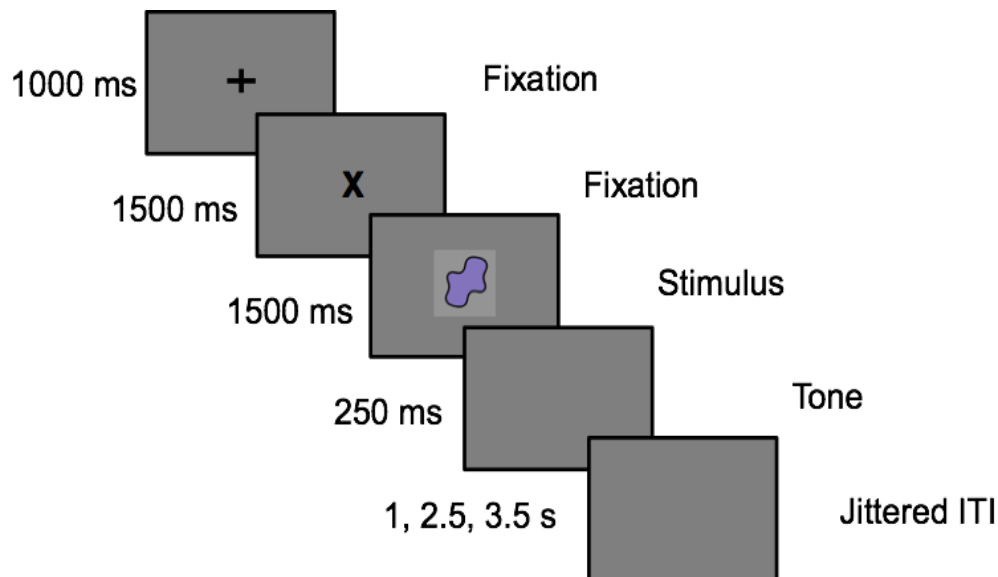
266 In a recent paper (Wijeakumar et al., 2015), we contributed to this fMRI literature
267 by examining whether response selection and inhibition areas in the brain are active
268 primarily on inhibitory trials as some researchers have claimed (Aron, Robbins, &
269 Poldrack, 2014), or, alternatively, whether response selection and inhibition areas are
270 active when salient events occur, regardless of whether these events require inhibition
271 per se (Erika-Florence, Leech, & Hampshire, 2014; Hampshire & Sharp, 2015). To
272 contrast these views, we had participants complete a set of classic inhibitory control tasks
273 in an MRI scanner. We varied whether events were excitatory (i.e., required a motor
274 response) or inhibitory, and whether events were frequent or infrequent. We were
275 particularly interested in the brain response on infrequent, excitatory trials. The inhibitory
276 network view suggests that key areas of a fronto-cortical-striatal network should show a
277 weak response on these trials because no inhibition is required. The salience network
278 view suggests the opposite--that there should be a robust fronto-cortical-striatal network
279 response because infrequent events stand out as salient.

280 We used the data from Wijeakumar et al. (2015) as our case study in the present
281 report. We do this for two reasons. First, this is a convenient choice because we have the
282 full dataset, we are aware of all the processing details, and so on. Second, although there
283 are numerous other studies we could have picked, this one has some unique features.
284 Most notably, the study of Wijeakumar et al. has parametrically manipulated several

285 factors in the same task. This is good fodder to probe the potential of our model-based
286 approach because there is a lot of systematic patterning in the data to capture.

287 In the present report, we focus on data from one of the tasks from Wijekumar et
288 al. (2015)--a Go/Nogo (GnG) task. Participants were asked to press a button (Go) when
289 they saw some stimuli and withhold (Nogo) their response when another set of stimuli
290 were presented. Stimuli varied in color but not in shape. Go colors were separated from
291 Nogo colors by 60 degrees in a uniform hue space such that directly adjacent colors were
292 associated with different response types.

293



294

295 Figure 1. Experimental design for the GnG task.

296 Each trial started with a fixation cross presented at the center of the screen for
297 2500 ms, followed by the stimulus presentation at the center of the screen for 1500 ms
298 (see Figure 1). The participants were advised to respond to the visual stimuli as fast as
299 possible. If a response was not detected on the Go trials, then a message saying 'No
300 Response Detected' was presented on the screen for 250 ms. Inter-trial intervals were
301 jittered between 1000, 2500 or 3500 ms presented on 50%, 25% or 25% of the trials
302 respectively.

303 Two parametric manipulations were carried out – a Proportion manipulation and a
304 Load manipulation. For the Proportion manipulation (at Load 4), the number of Go and

305 Nogo trials were varied as follows. In the 25% condition, 25% of the trials were Go trials
306 and 75% of the trials were Nogo trials. In the 50% condition, 50% of the trials were Go
307 trials and 50% of the trials were Nogo trials. In the 75% condition, 75% of the trials were
308 Go trials and 25% of the trials were Nogo trials.

309 For the Load manipulation, 50% of the trials were Go trials and the rest were Nogo
310 trials. In the Load 2 condition, one stimulus (color) was associated with a Go response
311 and another with the Nogo response. In the Load 4 condition, two stimuli were associated
312 with a Go stimulus and two other stimuli with a Nogo response. In the Load 6 condition,
313 three stimuli were associated with the Go response and three stimuli with a Nogo
314 response. Participants completed five runs in the fMRI experiment: Load 2, Load 4 (also
315 called Proportion 50), Load 6, Proportion 25 and Proportion 75. Each run had a total of
316 144 trials. The order of the runs was randomized.

317 fMRI data were collected using a 3T Siemens TIM Trio magnetic resonance
318 imaging system with a 12-channel head coil. An MP-RAGE sequence was used to collect
319 anatomical T1-weighted volumes. Functional BOLD imaging was acquired using an axial
320 2D echo-planar gradient echo sequence with the following parameters: TE=30 ms,
321 TR=2000 ms, flip angle= 70°, FOV=240Å~240 mm, matrix=64Å~64, slice
322 thickness/gap=4.0/ 1.0 mm, and bandwidth=1920 Hz/pixel.

323 The task was presented to the participant inside the scanner through a high-
324 resolution projection system connected to a PC using E-prime software. The timing of the
325 stimuli being presented was synchronized to the MRI scanner's trigger pulse. Head
326 movement was prevented by inserting foam padding between the participants' heads and
327 the head coil. Participants' responses were obtained through a manipulandum strapped
328 to the participants' hand.

329 Data were analyzed using Analysis of Functional NeuroImages (AFNI) software
330 (<http://afni.nimh.nih.gov/afni>). DICOM images were converted to NIFTI images. Voxels
331 containing non-brain tissue were stripped from the T1 structural image. The T1 structural
332 image was aligned to the Talaraich space. Then, EPI data was transformed to align with
333 the T1 structural scan in the subject-space. Transformation matrices across both these

334 steps were concatenated and applied to the EPI data to move it from subject-space to
335 Talaraich space. Six parameters for head movement were estimated (X, Y, Z, pitch, roll,
336 and yaw directions) for use as regressors to account for variance in the BOLD signal
337 associated with motion. Spatial smoothing was performed on the functional data using a
338 Gaussian function of 8mm full-width half-maximum.

339 Results showed a robust neural response in key areas of the fronto-cortical-striatal
340 network on infrequent trials regardless of the need for inhibition (Wijeakumar et al., 2015).
341 Interestingly, the number of stimulus-response (SR) mappings modulated the neural
342 signal across multiple brain areas, with a reduction in the BOLD signal as the number of
343 SR mappings increased. We suggested that this might reflect competition among
344 associative memories of the SR mappings as the SR load increased, consistent with
345 recent proposals (Cisek, 2012) and modeling work by Erlhagen and colleagues (Erlhagen
346 & Schöner, 2002).

347 In the next section, we present an overview of a dynamic neural field model
348 designed to capture both the behavioral and neural dynamics that underlie performance
349 in this study. Note that we use the model primarily in a tutorial fashion--to illustrate the
350 model-based fMRI approach using dynamic neural fields. Critically, we make no claims
351 that this is an optimal model of response selection. There are other more comprehensive
352 models of inhibitory control in the literature. For instance, Wiecki and Frank's model of
353 response inhibition unifies many findings from the inhibitory control literature and has
354 simulated key aspects of neural data from both neurophysiology and evoked-response
355 potentials (Wiecki & Frank, 2013). We think our model has some interesting strengths
356 relative to Wiecki and Frank's model that we highlight below, but it also has some
357 interesting limitations that we also highlight. These strengths and limitations are useful in
358 a tutorial style paper like this to illustrate the range of issues one must consider when
359 pursuing an integrative cognitive neuroscience model.

360 **4. A dynamic neural field model of response selection**

361 A key question one must ask when modeling even the most basic of tasks is what
362 perceptual, cognitive, and motor processes one should try to capture in the model and

363 what aspects should be left out in the interest of simplicity. In mathematical psychology,
364 such issues are central given that model simplicity versus complexity--often indexed by
365 the number of free parameters--is a key dimension along which models are compared.
366 The GnG task is relatively simple; thus, we can articulate the set of possibilities. One
367 could consider modeling the following: (1) the early visual processes that perceive and
368 encode colors presented in the visual field; (2) the attentional processes that selectively
369 attend to the presented color; (3) the memory and visual comparison processes that
370 identify whether the presented color is from the Go or Nogo set; (4) the response selection
371 processes that compete to drive a Go or Nogo decision; (5) the motor planning processes
372 that are activated, either partially or wholly by the response selection system; and (6) the
373 motor control processes that do the job of pushing the response button in the event of a
374 Go decision (whether correct or not).

375 In cognitive modeling of the GnG task, models typically focus on the heart of this
376 list--the response selection processes. Classic race-horse models (Boucher, Palmeri,
377 Logan, & Schall, 2007; Logan, Yamaguchi, Schall, & Palmeri, 2015), for instance, capture
378 many aspects of reaction time (RT) distributions from the GnG task using an elegant set
379 of simple equations. These models have also generated interesting neural predictions.
380 More complex models have also considered aspects of the memory and visual
381 comparison processes that underlie performance in this task (Wiecki & Frank, 2013). The
382 Wiecki and Frank model, for instance, used a set of SR associations in a complex neural
383 network to implement these memory and visual comparison processes. This added
384 complexity was justified because their goal was to mimic properties of the neural systems
385 that underlie response selection.

386 Our goal in the present report was to build a neural dynamic model of response
387 selection that captures the processes that underlie the GnG task from perception to
388 decision--to create an integrated neural architecture to capture processes 1-4 in the list
389 above. (Links to motor planning and control systems have been studied extensively with
390 DFT, but we opted for simplicity on this front; for discussion, see Schöner et al., 2015;
391 Bicho & Schöner, 1997.) We did this for two central reasons. First, we have proposed and

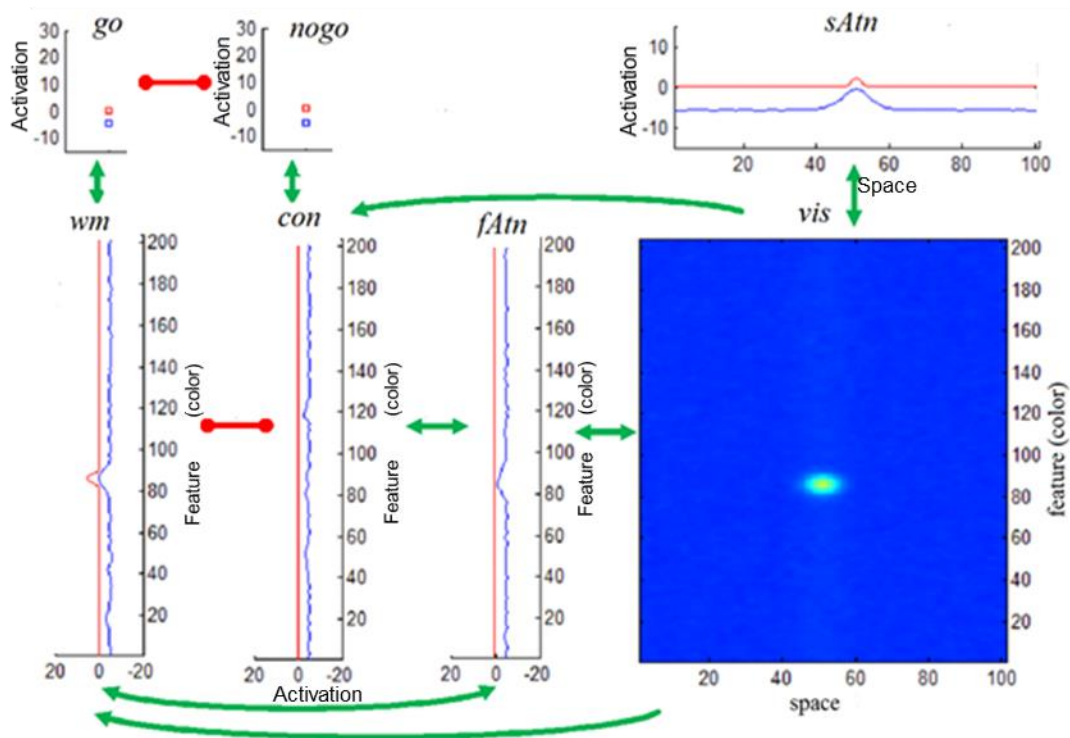
392 tested models that capture the full sweep of processes 1-4 in the domain of VWM; thus,
393 we wanted to examine whether the processes that underlie performance in VWM tasks
394 might also play a role in response selection. This is important theoretically, because it
395 probes the generality of a theory--can a theory instantiated in a particular architecture and
396 designed to capture data from one domain, quantitatively capture data from a different
397 domain of study? If so, this suggests that the model has the potential to integrate findings
398 across domains provided, of course, that the model is constrained and unable to capture
399 findings that are *not* present in those domains. Note that answering this question requires
400 deep study of the theory in question. We do not do that work here; rather, the present
401 paper is merely a first step in this direction.

402 The second reason stems from Buss et al. (2013) where we used a dynamic neural
403 field model to simulate fMRI data from a dual-task paradigm. In that project, we
404 discovered that non-neural inputs to the model--for instance, a perceptual input applied
405 directly to a higher-level processing area--often dominated the neural activation patterns,
406 thereby dominating the model-based MRI signals as well. This suggests that it is
407 important to embed the neural processes of interest within a fully neural system if you
408 want to capture neural dynamics in a reasonable way. Concretely, this means that we had
409 a priori reasons for simulating early perceptual and attentional processes in the model,
410 even though most models do not do this in the interest of simplicity.

411 4.1 Conceptual overview and model architecture

412 With that background in mind, Figure 2 shows the architecture of the model. This
413 model is an integration of several models developed to simulate findings from VWM tasks
414 (Johnson et al., 2009; Johnson et al., 2009; Schneegans et al., 2014; Schöner et al.,
415 2015), consistent with our goal of asking whether a model of VWM can generalize to a
416 response selection task. We describe the architecture in detail below, pointing out links
417 to prior work to justify why we have used this particular architecture here. Note that each
418 element in Figure 2 is a dynamic neural field. We provide the full mathematical
419 specification of a dynamic neural field in the next section.

420 The model has a visual field in the lower right panel that mimics properties of early
 421 visual cortical fields (Markounikau, Igel, Grinvald & Jancke, 2008). The visual field is
 422 composed of neural sites receptive to both color (hue) and spatial position. Inputs into
 423 this field build localized 'peaks' of activation in the two-dimensional field that specify the
 424 color of the stimulus and where it is located. These peaks, in turn, drive activation--in
 425 parallel--in the fields along a ventral feature pathway shown in the bottom row of Figure
 426 2 (see fAtn, con, wm) and in a dorsal pathway in the top right panel (see sAtn). Two of
 427 these fields are 'winner-take-all' attentional fields that selectively attend to the color of the
 428 presented item (feature attention or fAtn) or its spatial position (spatial attention or sAtn).
 429 These fields do not have much to do in the GnG task because only a single item is
 430 presented centrally in the visual field; they are included here for continuity with previous
 431 models (Schneegans et al., 2014; Schöner et al., 2015) and to pass neurally-realistic
 432 inputs to the other cortical fields.



433

434 Figure 2. Architecture of the GnG DNF model. Seven sub-networks are included: (i) the visual
435 field, vis; (ii) the spatial attention field, sAtn; (iii) the feature attention, fAtn; (iv) the contrast field,
436 con; (v) the working memory field; wm; (vi) the go and (vii) nogo nodes. The neural fields are
437 coupled by uni- or bi- directional excitatory (green) or inhibitory (red) connections. Within each
438 field, the activation variable $u(x, t)$ at a given time instance $t = \tilde{t}$ is plotted in blue. Field output
439 $g(u(x, t))$ at $t = \tilde{t}$ is in red. The range $[-20, 20]$ (horizontal axis for fAtn, con, wm), or $[-15, 15]$, $[-$
440 $15, 30]$ (vertical axis for sAtn, go, Nogo) show values taken by activations and field outputs.
441 Feature (color) and space dimensions have a span of 204 units (vertical axes in the lower panels)
442 and 101 units (horizontal axes in upper and lower right panels) respectively.

443

444 The more interesting fields are 'higher up' in the ventral pathway, where the model
445 must decide whether the presented color is from the Go set or the Nogo set. This requires
446 some form of memory--the system has to remember the details of the Go and Nogo set
447 (see Logan et al., 2015 for evidence that the Nogo set is remembered)--and some form
448 of visual comparison--the system has to visually compare the hue value of the presented
449 color to the memorized options. The reciprocally inhibitory architecture instantiated in the
450 working memory (wm) and contrast (con) fields implements this visual comparison
451 process (see Johnson et al., 2009; Johnson et al., 2009). This piece of the architecture
452 has been tested in several previous studies including tests of novel behavioral predictions
453 (see Johnson et al., 2009). Moreover, this core approach to visual comparison has been
454 generalized to visual comparison tasks in infancy as well (Perone & Spencer, 2013;
455 Perone & Spencer, 2013, 2014). To this, we add a memory trace mechanism that
456 remembers the colors previously consolidated in working memory (mem_wm) and the
457 colors previously identified as 'contrasting' with the go set in the contrast field (mem_con)
458 (Lipinski, Schneegans, Sandamirskaya, Spencer, & Schöner, 2012; Perone, Simmering,
459 & Spencer, 2011; Schutte & Spencer, 2002).

460 The final piece of the architecture implements the decision process. Here, we have
461 implemented two dynamical nodes--localized neural populations (Schöner et al., 2015) -
462 - that compete in a winner-take-all manner to make a Go or a Nogo decision. The go node
463 receives the summed activation from the working memory layer. Conceptually, if the

464 working memory layer detects a match between the remembered set of Go colors (in the
 465 memory trace) and the current color detected in the feature attention and visual fields,
 466 this layer will build a peak of activation, consolidating the item in working memory and
 467 passing strong activation to the go node (Figure 3A). Alternatively, if the contrast layer
 468 detects a match between the remembered set of Nogo colors--the items that contrast with
 469 the Go set--and the current color detected in the feature attention and visual fields, this
 470 layer will build a peak of activation and send strong activation to the nogo node (Figure
 471 3B). Conceptually, the winner in the race between Go and nogo nodes would then drive
 472 activation in the motor system (which we do not implement here).

473 In the section below, we provide a more formal treatment of the dynamic neural
 474 field model. We also walk through an example to illustrate the neural population dynamics
 475 in the model that give rise to an in-the-moment decision to make a Go decision or to inhibit
 476 responding via a Nogo decision.

477 4.2 Formal specification of the model and exemplary simulations

478 The model consists of several dynamic neural fields (DNFs) that compute neural
 479 population dynamics u_j according to the following equation (Amari, 1977; Ermentrout,
 480 1998):

$$481 \quad \tau_e \dot{u}_j(x, t) = -u_j(x, t) + h_j + [c_j * g_j(u_j)](x, t) + \sum_k [c_{jk} * g_k(u_k)](x, t) + \eta_j(x, t) \\ 482 \quad + s_j(x). \quad (4.1)$$

483
 484 The activation u_j of each component is modeled at high temporal resolution (millisecond
 485 timescale) with time constant τ_e . It assumes a resting level h_j and depends on lateral
 486 (within the field) and longer range (between different fields) excitatory and inhibitory
 487 interactions, $c_j * g_j(u_j)$ and $c_{jk} * g_k(u_k)$ respectively. These are implemented by
 488 convolutions between field outputs $g(u(x, t))$ and connectivity kernels $c(x)$ with the latter
 489 defined either as a Gaussian function or as the difference of two Gaussians ("Mexican
 490 hat" shape). The temporal dynamics of the neural activity is also influenced by external
 491 inputs s_j and it is non-deterministic due to noise η_j .

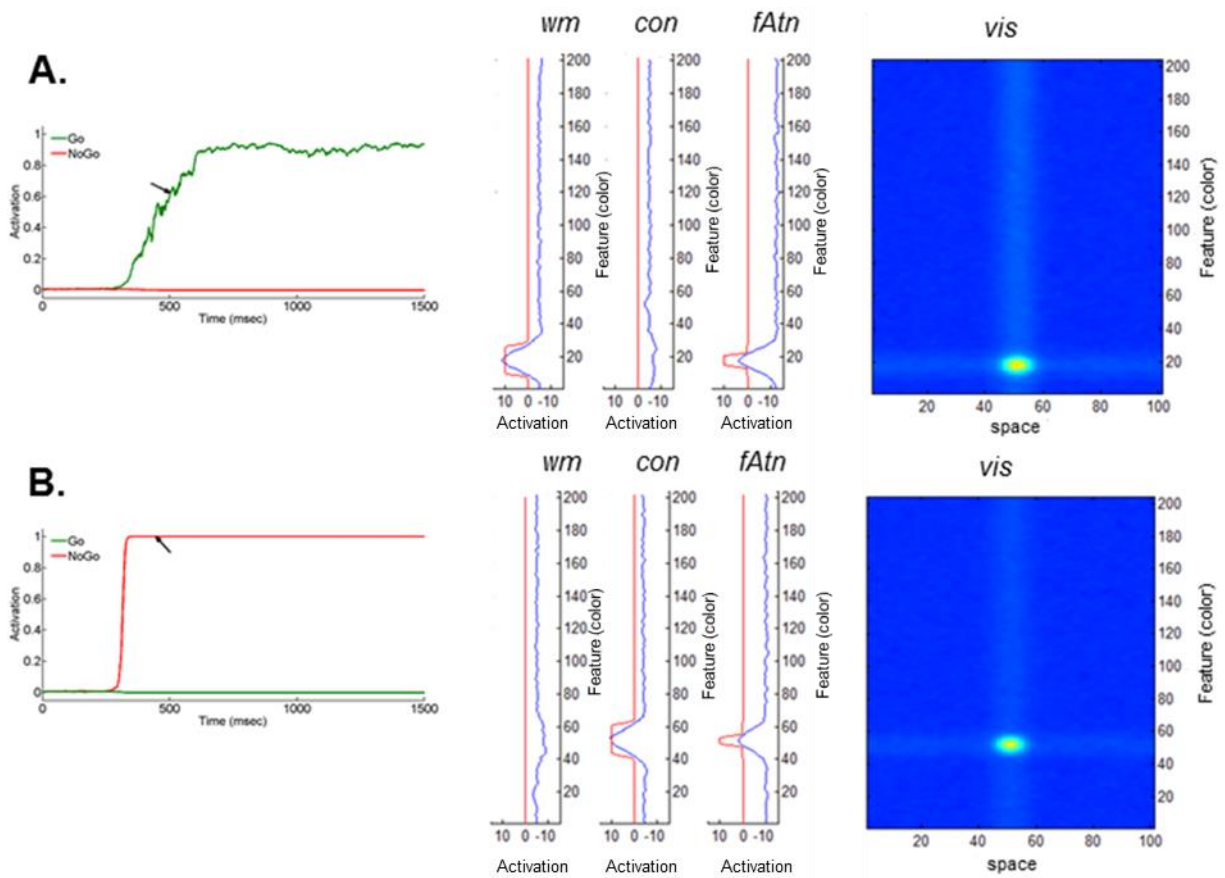
492 The activation $u(x, t)$ is distributed continuously over an appropriate feature space
493 x such as color or spatial position (Figure 2 – blue curves). Then the field output,
494 $g(u(x, t))$, is computed by the sigmoid (logistic) function $g(u) = 1/(1 + \text{Exp}[-\beta u])$ with
495 threshold set to zero and steepness parameter β (Figure 2 – red curves). Therefore,
496 $g(u)$ remains near zero for low activations; it rises as activation reaches a soft threshold;
497 and it saturates at a value of one for high activations. Excitatory and inhibitory coupling,
498 both within fields and among them, promote the formation of localized peaks of activation
499 in response to external stimulation. In our model, any above-the-threshold activation peak
500 is interpreted as an experimentally detectable (via neural recordings) response of that
501 particular neural field to a stimulus.

502 The architecture of the dynamic neural field model includes the seven fields shown
503 in Figure 2. (For details on field equations and parameter values, see Appendix A.) A time
504 snapshot of the dynamics of the DNF model during a Go/Nogo task is shown in Figure 3.
505 (The time instance \tilde{t} is approximately 500 ms after stimulus onset, and it is indicated on
506 the graph by a black arrow).

507 Figure 3A illustrates the network state of the DNF model at time \tilde{t} during the Go
508 task. The parameter values used in simulations are listed in Appendix A (Model 1 for Load
509 2 condition). Shortly, when a Go color is presented (duration of stimulus is 1500 ms), an
510 activation peak is built in the visual field, vis. This induces a peak in the working memory
511 field, wm, and a weak peak in the feature attention field, fAtn (curves in blue). Then, the
512 peak in wm leads to an increase in activation of the go node (Figure 3A; in green). In
513 addition, due to inhibition from wm that dominates excitation received from vis, the activity
514 of the contrast field, con, is lowered at the location of the Go color. At some time between
515 400 and 500 milliseconds after stimulus onset, the activity of the go node crosses the
516 threshold, that is, its output function is greater than 0.5 (see left panel; in green). This is
517 caused by the formation of a strong peak in wm. In addition, the peak in fAtn becomes
518 stronger and a sub-threshold hill forms in con as well. In the interval of time between the
519 response (reaction time RT~ 450 ms) and end of the trial (1500 ms), the activity peaks in

520 vis, fAtn, con and wm stabilize. Importantly, the hill in con remains sub-threshold. Also,
 521 note that the activity of the go node reaches saturation.

522 Figure 3B shows the network state of the DNF model at time \tilde{t} during the Nogo
 523 task. In this case, the Nogo color induces activation of the visual field, vis. This, in turn,
 524 increases activation in the contrast field, con, at the corresponding color coordinate along
 525 the feature space. A sub-threshold hill in fAtn forms as well, and wm is locally inhibited.
 526 Then, later during the trial (e.g. at time \tilde{t}), the activation of the nogo node has crossed its
 527 threshold. The peak in con becomes stronger and stabilizes, and field fAtn shows supra-
 528 threshold activity. At the Nogo color location in wm, the activity is inhibited. Approaching
 529 the end of the trial, the activity stabilizes in vis, fAtn, con and wm, the peak in wm
 530 remaining sub-threshold. Note that the nogo node stays 'on', while the go node remains
 531 inactive.



532

533 Figure 3. Network state of the DNF model at time instance \tilde{t} , approximately 500 ms after stimulus
534 onset, during: (A) Go task and (B) Nogo task (only vis, fAtn, con, wm are shown). Time evolution
535 of the output of go (in green) and Nogo (in red; left panel) nodes is also shown. Time \tilde{t} is indicated
536 by the black arrow. Simulations used parameters from Appendix A (see Model 1 and Load 2
537 condition).
538

539 **5. Simulating behavior with the dynamic neural field model**

540 When contrasted with cognitive models, the dynamic neural field model in Figure
541 2 is complex. Each field has several parameters that need to be 'tuned' appropriately to
542 get the model to perform in a manner that is consistent with our hypotheses about how
543 response selection works. When contrasted with biophysical neural network models,
544 however, the dynamic neural field model is relatively simple--there are fewer neural sites
545 and far fewer free parameters. Along this dimension of complexity, therefore, DFT sits
546 somewhere in the middle. That is by design. We contend that using neural process
547 models is critical in psychology and neuroscience because this opens the door to
548 important constraints for theory from both behavioral and neural measures--constraints
549 readily apparent when one tries to construct integrative cognitive neuroscience models.
550 In our view, these constraints justify the complexity. At the same time, we think it is
551 important to add just the right amount of complexity. Data from neurophysiology suggest
552 to us that perception, cognition, and action planning live at the level of neural population
553 dynamics, and not at the biophysical level per se (for discussion, see (Gregor Schöner et
554 al., 2015). Thus, we contend that the added detail from biophysical models is not critical
555 if the goal is to bridge the gap between brain and behavior.

556 Of course, the downside to the added complexity introduced by dynamic neural
557 field models is that fitting data to behavioral and neural data becomes harder and a bit
558 more subjective in nature. This is not to say that DFT cannot achieve quantitative fits--
559 that is certainly still a goal. Rather, the subjective sense of DFT comes from the fact that
560 it is rarely possible to search the full parameter space of a dynamic neural field model.
561 Consequently, many of the issues that are central to mathematical psychology and many
562 of the tools that are used to evaluate model fits (Turner et al., 2016) are difficult, if not
563 impossible, to apply to dynamic neural field models (Samuelson et al., 2015).

564 Critically, however, fitting dynamic neural field models to data is not an
565 unconstrained free-for-all. Rather, constraints come from multiple sources. First, the
566 neural dynamics in the model must reflect our understanding of how brains work. Thus,
567 we would rule out parameters that give rise to pathological neural states. For instance, if

568 excitatory neural interaction strengths in one of the cortical fields are too strong, input to
569 the field will build a peak that grows out of control--the model has a seizure. By contrast,
570 if excitatory neural interaction strengths are too weak, no peaks will build--the model will
571 remain in a sub-threshold state.

572 Second, parameters must be tuned such that the neural dynamics reflect our
573 conceptual theory of how the model should behave in the task. Concretely, this means
574 that the right sequence of peaks emerges during the course of a trial to give rise to the
575 right type of behavior (in this case, the generation of a Go or Nogo decision). Formally,
576 this means that the sequence of bifurcations in the model must be correct. For instance,
577 the following should hold: (1) peaks in the working memory and contrast fields should not
578 build spontaneously from a memory trace; (2) peaks in the working memory and contrast
579 fields should be influenced by the formation of peaks in feature attention (that is, the
580 parallel input from the visual field should not be too strong); and (3) the Go and Nogo
581 competition should be influenced by sub-threshold activation in the working memory and
582 contrast fields as decision-making unfolds.

583 The third category of constraint comes, of course, from the details of behavioral
584 data. In the GnG task, these constraints are relatively modest since the participant only
585 responds on Go trials. Nevertheless, if one considers RT distributions rather than just
586 means, this can be relatively constraining. For instance, Erlhagen and Schöner fit the
587 details of response distributions from several response selection paradigms (Erlhagen &
588 Schöner, 2002). This is possible with dynamic neural field models because such models
589 are stochastic, and they generate measurable behaviors on every trial (e.g., the formation
590 of a stable Go or Nogo decision). Moreover, relatively complex models as the one used
591 here generate complex non-linear patterns through time--for instance, a sequence of
592 peak states across fields, which can amplify stochastic fluctuations leading to
593 macroscopic behavioral differences across conditions. Further behavioral constraints
594 emerge when one considers response distributions from multiple studies. Here, the goal
595 would be to capture the quantitative details of behavioral responses from multiple studies,
596 ideally without any modification to model parameters. This has been achieved in several

597 notable cases (Buss & Spencer, 2014; Erlhagen & Schöner, 2002; A.R. Schutte &
598 Spencer, 2002).

599 Here, our goals were more modest--we did not optimize the quantitative fit to the
600 behavioral data. Rather, we pursued a more iterative parameter fitting approach. First,
601 we fit the mean reaction times with the dynamic neural field model, and made sure the
602 variance in the model was in the right ballpark. We refer to this as **Model 1** (see Appendix
603 A). As readers will see, our fits to the standard deviations could have been better;
604 however, we did not optimize the model on this front. Rather, we pushed forward to
605 evaluate the quantitative fMRI fits first. Data from these fits revealed that Model 1 did not
606 quite outperform the quantitative fit provided by a **Standard GLM analysis** -- the 'gold
607 standard' statistical model we set a priori. We then examined the model's neural data,
608 focusing on the ways in which the model's neural dynamics differed from the neural
609 dynamics evident in the fMRI data (see Wijekumar et al., 2015). This led to new insights
610 into how we had the model parameters 'tuned' and prompted a second round of
611 behavioral fits targeting more competitive neural interactions. This resulted in a second
612 set of parameters--**Model 2** (see Appendix A)--that fit the behavioral data relatively well
613 and fit the fMRI data better than Model 1. This illustrates how an interactive cognitive
614 neuroscience approach can be used in practice to bridge the gap between brain and
615 behavior.

616 5.1 Simulation methods

617 Before turning to the details of the behavioral fits, we provide a few more details
618 about the simulation method. All numerical simulations were performed using the
619 COSIVINA simulation package (available at www.dynamicfieldtheory.org). This package
620 allows one to construct dynamic neural field architectures relatively quickly, along with a
621 graphic user interface that enables evaluation and 'tuning' of the model in real time (see
622 Figures 2-3). The same simulator can then be run in 'batch' mode to iterate the model
623 across many trials, recording responses that can be evaluated relative to empirical data.
624 The COSIVINA package also includes a new toolbox for generating local field potentials
625 directly from the model at the same time that the model is simulating the experimental

626 task. Thus, the model is truly an integrative cognitive neuroscience model, generating
627 behavioral and neural data (with millisecond precision) simultaneously.

628 5.1.1 Parameter fitting in Model 1

629 We adopted the following approach when tuning model parameters to arrive at
630 Model 1. First, we made a simplification of the model. Initial simulations with a dynamic
631 memory trace in both the working memory and contrast fields showed that the memory
632 trace dynamics conformed to expectations based on previous work (Buss et al., 2013;
633 Erlhagen & Schöner, 2002; Lipinski et al., 2010). In particular, memory traces were
634 stronger in the Load 2 condition and weaker in the Load 6 condition. This occurs because
635 each color is presented more often over trials in Load 2. Similarly, memory traces were
636 stronger for Go stimuli in the Proportion 75% condition and weaker in the 25% condition.
637 Again, this mimics the frequency of stimulus presentation. Although these memory trace-
638 -or learning--dynamics are fundamentally interesting, they also make simulation work
639 more complex because one must simulate a variety of stimulus presentation orders to
640 obtain robust estimates of learning effects. Given that such learning effects--in both
641 behavioral and fMRI data--were central to our previous work using an interactive model-
642 based fMRI approach (Buss et al., 2013), we opted to simplify the learning dynamics here.
643 Thus, instead of simulating memory traces dynamically over trials, we used static memory
644 traces, that is, the memory trace inputs were fixed for each condition to reflect the
645 properties revealed by these initial simulations (see equation A.17 and Table A.4.1 in
646 Appendix A, for details).

647 The next objective was to find a set of parameters that quantitatively captured data
648 from the Load 2 condition. We started with parameters from Schöner, Spencer and the
649 DFT Research Group (2015; Chapter 8), and adjusted the model parameters to
650 approximate the right behavior from the Load 2 condition. For instance, connection
651 strengths between the *go* node and *wm* field and *nogo node* and *con* field were tuned.
652 The strength of the memory trace inputs into the *wm* and *con* fields for Go and Nogo trials
653 respectively, were tuned as well.

654 Once the model captured the reaction times for Go trials at Load 2, the next step
655 was to capture reaction times for the Load 4 and Load 6 conditions. Here, we
656 hypothesized that increasing the Load in the task would increase competition among
657 memory traces, slowing down the time it takes to build a peak in the working memory and
658 contrast fields and yielding slower reaction times (Erlhagen & Schöner, 2002), Hence, we
659 adjusted the strength of the memory trace inputs in both *wm* and *con* fields without
660 modifying any other parameters. (See Table A.4.1 in Appendix A; third column shows
661 how the strength of the memory trace inputs for *wm* and *con* is varied across different
662 conditions.) We then tested whether the model was able to capture the increase in
663 reaction times observed as memory Load increased.

664 For the Proportion manipulation, Proportion 50% corresponded to Load 4 and so
665 its parameters were used as an anchor to fit the reaction times from Proportion 25% and
666 Proportion 75%. Here, we hypothesized that as the number of Go trials increased, the
667 strength of the memory trace for Go trials would also increase. Likewise, as the number
668 of Go trials decreased, the strength of these memory traces would decrease. (Table A.4.1
669 in Appendix A).

670 To generate quantitative data from the model, we ran 144 trials per model and 20
671 identical models (to reflect the number of participants in the original study) for each of the
672 Load and Proportion manipulations. Mean and standard deviations were calculated
673 across reaction times and compared to the empirical data (Figure 4).

674 5.1.2 Parameter fitting in Model 2

675 To identify parameters for Model 2, we proceeded as follows. After discovering that
676 Model 1 did not meet our quantitative criterion for fits to the fMRI data, we examined the
677 neural predictions from the model across conditions relative to fMRI results from
678 Wijeakumar et al. (2015). A central effect in Wijeakumar et al. was that regions of the
679 fronto-cortical-striatal network showed greater activation on infrequent trials, regardless
680 of whether an infrequent stimulus appeared on a Go or Nogo trial (Wijeakumar et al.,
681 2015). For instance, brain areas responded strongly on infrequent Go trials. Quantitative
682 fMRI predictions from Model 1 did not show this pattern. Given that local field potentials

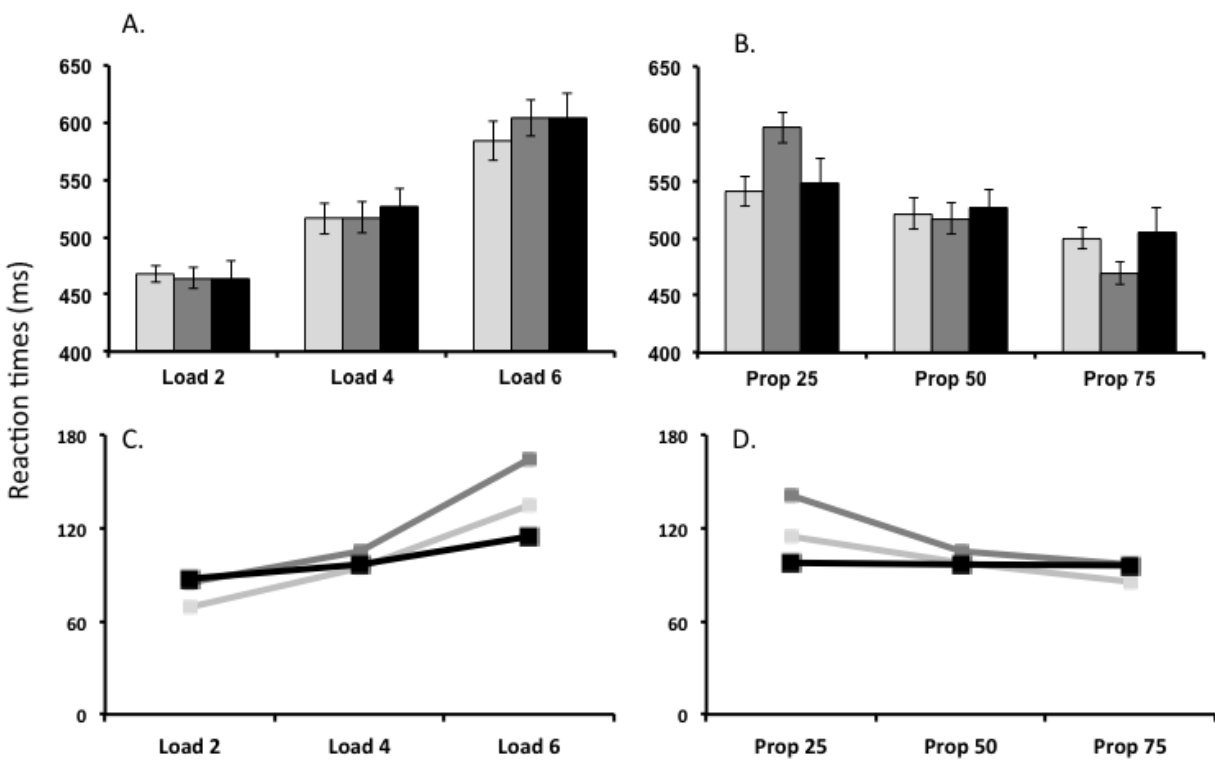
683 are positively influenced by both excitatory and inhibitory interactions, we hypothesized
684 that a strong response on infrequent Go trials might be most likely to occur when there is
685 a strong memory of frequent Nogo responses and strong competition between the
686 working memory and contrast fields (and vice versa on infrequent Nogo trials). To
687 examine this possibility, we added a new element to the model--a memory trace to the go
688 and nogo nodes (implemented by modulating the gain on self-excitation across
689 conditions, see Table A.2.1 in Appendix A) and we increased competition between the
690 wm and con fields (Table A.3.1). We also balanced the parameters across the go and
691 Nogo systems, setting the reciprocal connections between nogo node and con field so
692 they were equal to the parameters connecting go node and wm field (Table A.3.1).

693 Our examination of the model's neural dynamics also revealed that differences
694 across conditions were relatively modest. We realized that this was influenced by the trial
695 duration we were simulating. Decisions in the model--and decisions by participants--occur
696 within the first 500ms; for the remaining 1000ms, the model simply sits in a neural attractor
697 state, maintaining peaks across all fields (because the stimulus remains 'on'). Because
698 the BOLD signal reflects the slow blood flow response to all of these events, the 'final'
699 attractor states of the model dominate the hemodynamic predictions and the more
700 interesting cognitive processes--the neural interactions leading to the decision--have
701 relatively less impact. This does not accurately reflect neural systems; rather,
702 neurophysiological data suggest that neural attractor states stabilize, but are then
703 suppressed once a stable decision has been made (Annette Bastian et al., 2003). To
704 implement this, we added a 'condition of satisfaction' node (CoS), building off recent work
705 by Sandamirskaya and colleagues (Sandamirskaya & Schöner, 2008; Sandamirskaya,
706 Zibner, Schneegans, & Schöner, 2013; Gregor Schöner et al., 2015). This node receives
707 input from both the go and nogo nodes. When either becomes active, the 'CoS' node
708 becomes active, signalling that the conditions for a stable decision have been satisfied.
709 The CoS node then suppresses the working memory and contrast fields, globally
710 inhibiting these fields. Consequently, the stable decision made by the go or nogo node
711 remains active throughout the 1500ms trial, but peaks in the wm and con fields are

712 suppressed once the decision is made. Conceptually, this frees up these systems to move
713 on to other interesting events that might (but don't) occur in the visual field.

714 5.2 Quantitative behavioral results

715 Here, we present the results of the behavioral fits for Models 1 and 2 alongside the
716 reaction times from the actual behavioral data. Both DNF models provide reasonable fits
717 to the trends in reaction times shown by the behavioral data in response to manipulating
718 Proportion and Load (see Figure 4A and 4B). Root Mean Squared Error (RMSE) for
719 reaction times for Model 1 with respect to the Standard GLM analysis = 10.58ms and
720 RMSE for reaction times for Model 2 with respect to the Standard GLM analysis =
721 27.02ms. For the Load manipulation, reaction times increased as the number of SR
722 mappings increased. For the Proportion manipulation, increasing the frequency of Go
723 trials from 25% to 75% resulted in a decrease in reaction times. Although there were
724 some variations in the standard deviations across the 20 simulations for both models (as
725 shown in Figure 4C and 4D), the trends across the conditions were qualitatively correct.



726

727 Figure 4. (A-B) Mean reaction times computed for the DNF model (Model 1 shown in light grey
728 and Model 2 shown in dark grey) and behavioral data (shown in black) for the manipulation of the
729 (A) Load and (B) Proportion. (C-D) Mean standard deviations of reaction times across simulations
730 for the (Model 1 shown in light grey and Model 2 shown in dark grey) and behavioral data (shown
731 in black) for the manipulation of (C) Load and (D) Proportion.

732 **6. Generating local field potentials and hemodynamics from the DNF model**

733 To simulate the hemodynamics for this study, we adapted the model-based fMRI
 734 approach from Deco et al. (2004). Specifically, we created an LFP measure for each
 735 component of the model during each condition and tracked the LFPs in real time as the
 736 model simulated behavioral data. Then, we convolved the simulated LFPs with a gamma
 737 impulse response function to generate simulated hemodynamics, and as a result,
 738 regressors for each component and condition.

739 **6.1. Definition of the DNF model-based LFP**

740 To illustrate the procedure, we explain below the computation of the LFP for the
 741 contrast field neural population (*con* field in Figures 2-3). The LFPs for all other neural
 742 fields in the GnG DNF model (e.g. Model 1; see Figure 1) follow an identical approach.

743 Consider the dynamic field equation (4.1) with appropriate input neural fields and
 744 connections that contribute to the dynamics of the neural population in the *con* field. This
 745 equation is defined by (A.4) in Appendix A or, more explicitly, by

746

$$\begin{aligned}
 747 \quad \tau_e \dot{u}_{con}(y, t) = & -u_{con}(y, t) + h_{con} + s_{con}(y) + c_{con,noise} * \xi(y, t) \\
 748 \quad & + \left((c_{con,E} - c_{con,I}) * g_{con}(u_{con}) \right)(y, t) + \sum_{j=vis,fAtn,wm} c_{con,j} * g_j(u_j)(y, t) \\
 749 \quad & + a_{con,nogo} g_{nogo}(u_{nogo}(t))
 \end{aligned}$$

750 where $f * h$ denotes the convolution $f * h(y, t) = \int f(y - y')h(y', t)dy'$.

751

752 Here $s_{con}(y)$ specifies the stationary sub-threshold stimulus to the *con* field (“the memory
 753 trace”), spatially tuned to Nogo colors. The spatially correlated noise η_{con} is obtained by
 754 convolution between kernel $c_{con,noise}$ and vector ξ of white noise. Local connections
 755 include both excitatory and inhibitory components, $c_{con} = c_{con,E} - c_{con,I}$. All kernels are
 756 Gaussian functions of the form $c(y - y') = a \text{Exp} \left[-\frac{(y-y')^2}{2\sigma^2} \right]$ with positive parameters a
 757 except $a_{con,wm} < 0$. Note that, whenever Model 2 is used in simulations, an additional

758 term associated with feedback projections from the condition of satisfaction node (CoS)
 759 appears in u_{con} .

760 To generate an LFP for the contrast field, we sum the absolute value of all terms
 761 contributing to the rate of change of activation within the field, excluding the stability term,
 762 $-u_{con}(y, t)$, and the neuronal resting level, h_{con} . The resulting LFP equation for the *con*
 763 field is given by:

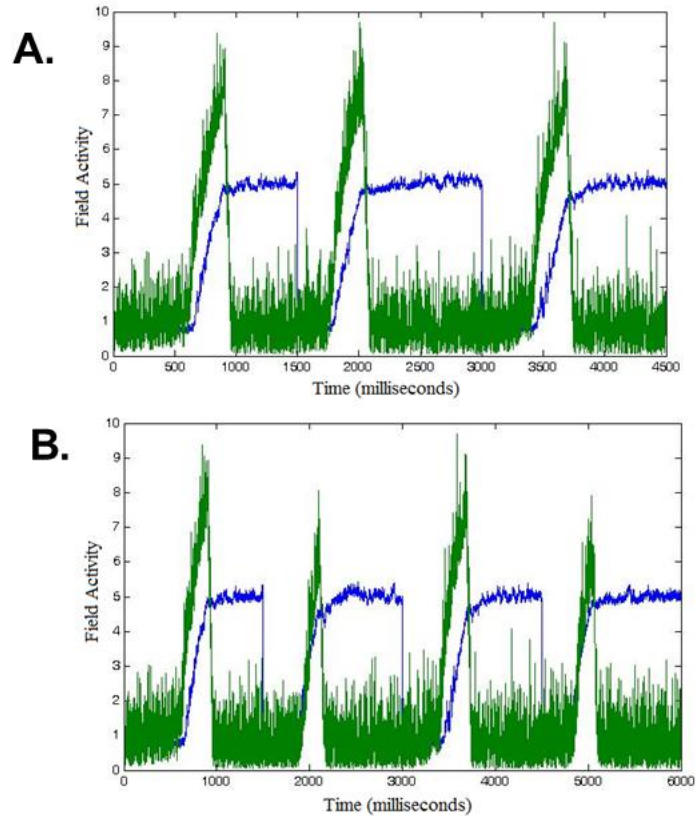
$$\begin{aligned}
 LFP_{con}(t) = & \frac{1}{n} \int |s_{con}(y)| + |c_{con,noise} * \xi(y, t)| dy \\
 & + \frac{1}{n} \int |c_{con,E} * g_{con}(u_{con})(y, t)| + |c_{con,I} * g_{con}(u_{con})(y, t)| dy + \\
 764 & + \frac{1}{n} \int |c_{con,fAtn} * g_{fAtn}(u_{fAtn})(y, t)| + |c_{con,wm} * g_{wm}(u_{wm})(y, t)| \\
 & + \frac{1}{n \times m} \int |c_{con,vis} * g_{vis}(u_{vis})(y, t)| dy + \\
 & + |a_{con,nogo} g_{nogo}(u_{nogo}(t))|
 \end{aligned}$$

765
 766 (6.1)

767 Several observations about this calculation need to be made. First, since both
 768 excitatory and inhibitory communication require active neurons and, biophysically,
 769 generate positive ion flow, we need to sum both in a positive way toward predictions of
 770 local activity; thus, we take the absolute value of all excitatory and inhibitory contributions.
 771 Second, given that field activities in the calculation of the LFP measure may span different
 772 dimensions, we normalize them. In this way, we can maintain a balance among their
 773 contributions. We do that by dividing each field contribution by the number of units in it
 774 (e.g., in equation (6.1) certain field contributions were divided by n or $n \times m$ where n is
 775 the feature dimension and m is the space dimension). Third, due to correlated noise in
 776 each field of the model, small-scale variations in the signal occur (especially evident in
 777 the second component), as well as overall variation in reaction times. Indeed, for same
 778 initial conditions, the DNF model yields relatively different LFP measures (see Figure 5A).

779 Each component in the model has a different network of interactions that drives a
 780 different response pattern. Consequently, individual LFP measures are created for each

781 model component, that is, for each of the 7 fields shown in Figure 2. Figures 5A and 5B
782 depict LFP simulations from fAtn and go node in Model 2, over three and four trials,
783 respectively.

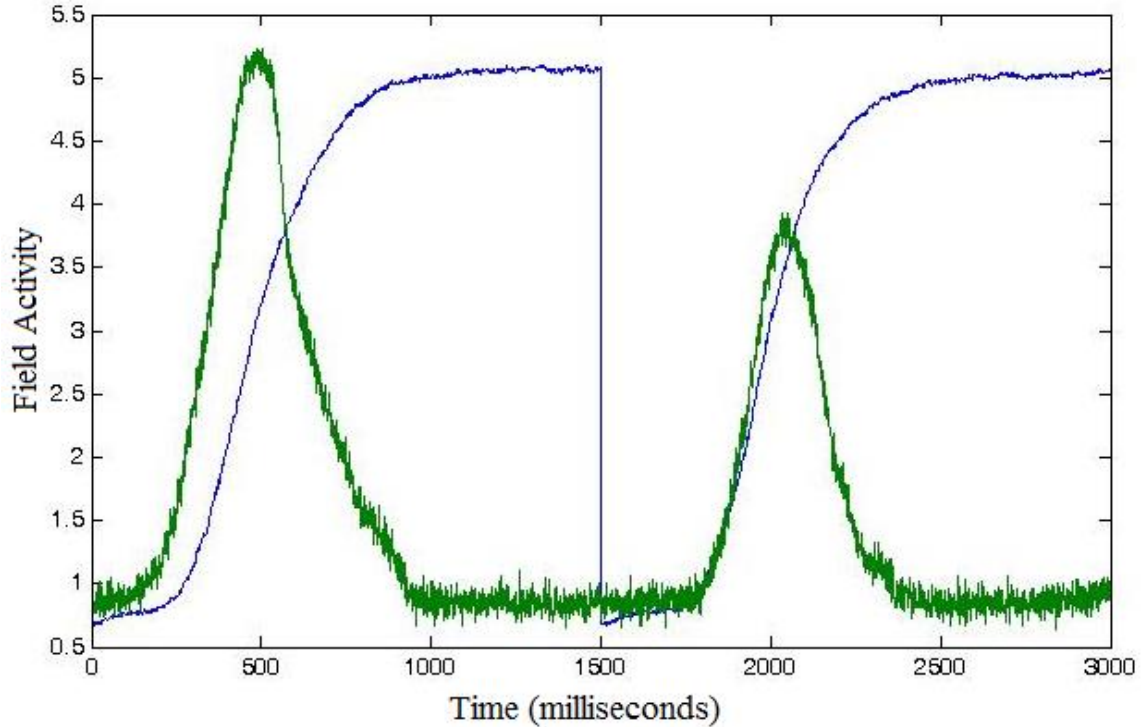


784
785 Figure 5. DNF-model-based LFPs computed for two fields in Model 2: feature attention (fAtn; in
786 blue) and go node (green). Different fields drive different response patterns. They are computed
787 under the following conditions: (A) Three repetitions (1500ms long each) of Load 4, Go trials, and
788 (B) Sequence of four trials at Load 4 with order Go-Nogo-Go-Nogo. The variance between the
789 repetitions is a consequence of the stochastic nature of the model.

790 6.2. Canonical predicted LFPs per experimental condition

791 Note that, in some components, the LFP level is similar across conditions
792 with minor differences in timing (fAtn). In others (go node), different conditions (Go
793 trial versus Nogo trial) lead to larger differences in the LFP (Figure 5B). This
794 contrast is key to the model-based approach because it allows components to
795 have unique signatures on both the scale of the individual trial as well as larger
796 scale signatures across task conditions.

797 To account for this variance, we run many repetitions of each condition (i.e.
798 we start from same initial values in the model; therefore, the variability will be a
799 direct consequence of noise only). The number of repetitions is chosen usually to
800 reflect the number of trials undertaken by the subjects in the actual experiment.
801 (For example, if in the experiment, each of 20 subjects underwent 72 Go trials for
802 Load 4, we will run 20 sets of 72 repetitions (simulations) of Model 2 with the
803 corresponding parameters for stimulus strength from Table A.4.1.) We then
804 average the generated LFP time series over repetitions of the same condition to
805 determine what we call the canonical predicted LFP signal per condition. Figure 6
806 depicts examples of such canonical LFP predictions for two fields, fAtn (in blue)
807 and go-node (in green). The first 1500 ms in Figure 6 shows the canonical LFP
808 predictions for Load 4, Go trials (e.g., as seen repeated in Figure 5A). The last
809 1500 ms shows the canonical LFP predictions for Load 4 Nogo trials.



810

811 Figure 6. Canonical predicted LFPs computed for two fields in Model 2: feature attention
 812 (fAtn; in blue) and go node (green). Different fields drive different response patterns. They
 813 are computed under the following conditions: (left; first 1500 ms) Load 4, Go trials, and
 814 (right, last 1500 ms) Load 4, Nogo trials.

815

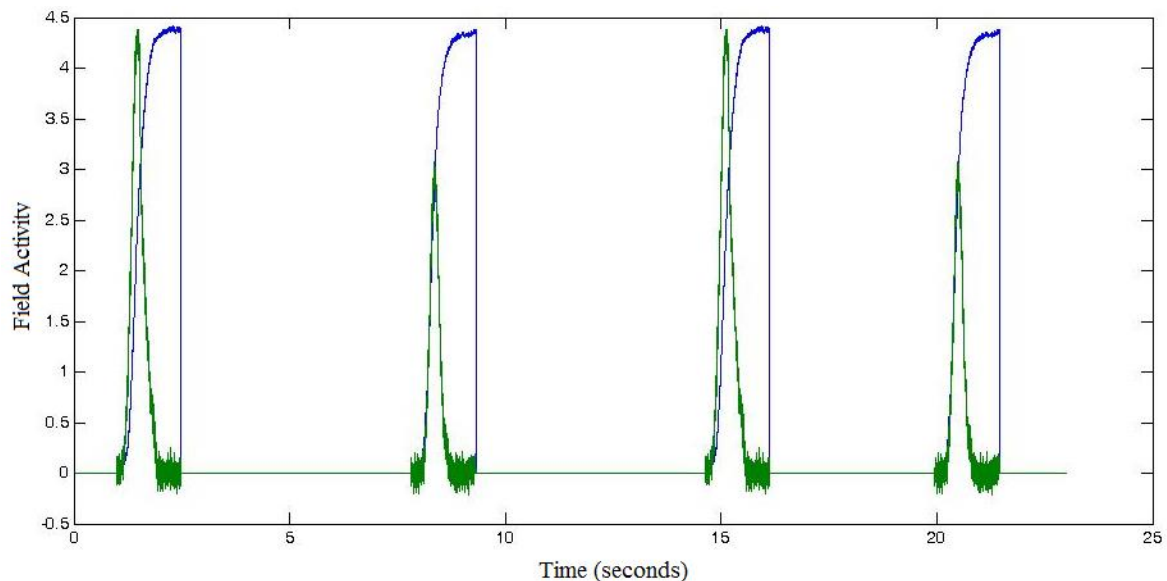
816 6.3. Construction of the long-form LFP template

817 Another concern that we aimed to address was placing the simulated
 818 canonical LFP values in an appropriate context. Much like the measurement of
 819 fMRI data, we take a baseline measurement from the model as follows. We use
 820 the same LFP calculations as described above, but we compute a "resting level"
 821 by simulating the model in the absence of external stimuli. We average these
 822 readings (across all time points and repetitions) to obtain an average resting value.
 823 Then, this value is subtracted out of our predictions to express the change in LFP
 824 activity relative to the resting value.

825 Once we have calculated a canonical baselined LFP for each model
 826 component and condition type, we proceed to construct long-form, averaged LFP
 827 templates. The latter are long-scale (tens of minutes) model-generated LFP
 828 predictions for each subject in the experiment. The structure of the long-form LFP

829 templates, for all components of the DNF model, is determined by the order and
830 timing of trials that particular subject experienced during the experimental block(s).

831 To do this, we first create a zero-valued time series the length of the entire
832 experiment (i.e. a zero-valued long-form LFP template). We then use trial onset
833 timings from the experiment to anchor the trial canonical baselined LFP prediction,
834 for each corresponding trial type. For example, if a trial of a certain condition (e.g.
835 Load 4, Nogo trial) has an onset time of 7500ms after the start of the experiment,
836 then the canonical LFP for that trial is inserted to the long-form template-LFP
837 starting at the same onset time (see Figure 7). Once this iterative process is
838 completed (across all trials) and the algorithm is applied to all DNF model
839 components, we have constructed experiment-based, subject-specific LFP time
840 series for each component of the DNF architecture. These time series reflect
841 predicted differences in neural activation based on the processes at work within
842 each field.



843
844 Figure 7. Excerpted long-form LFP templates computed for two fields in Model 2: fAtn
845 (blue) and go node (green). Depicted is an experimental block of four trials at Load 4,
846 presented to a particular subject in the ordered sequence Go-Nogo-Go-Nogo.

847

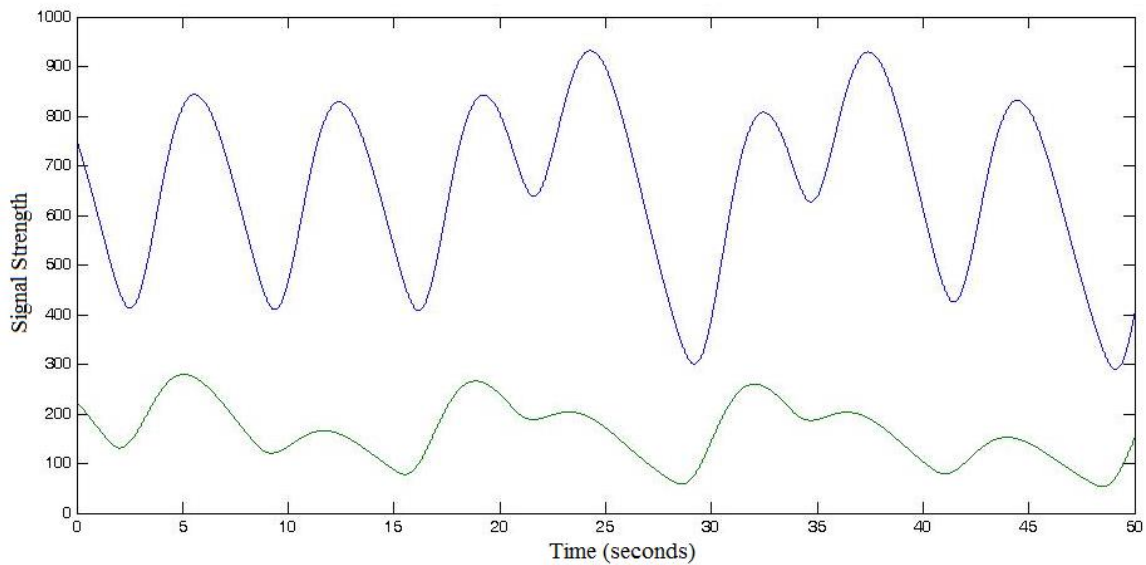
848 6.4. Generating hemodynamics from the DNF model

849 fMRI data does not measure neural activity directly. It measures changes in
850 blood flow as the neurovascular system responds to resource demands of active

851 neurons. Consequently, there is a delay between neural activity and the measured
 852 BOLD signal. To account for this, we use a standard hemodynamic response
 853 function,

$$854 \quad HRF(t) = \frac{t^{n-1}}{\lambda^n(n-1)!} \text{Exp}\left(-\frac{t}{\lambda}\right), \quad \lambda = 1.3 \text{ s}, \quad n = 4,$$

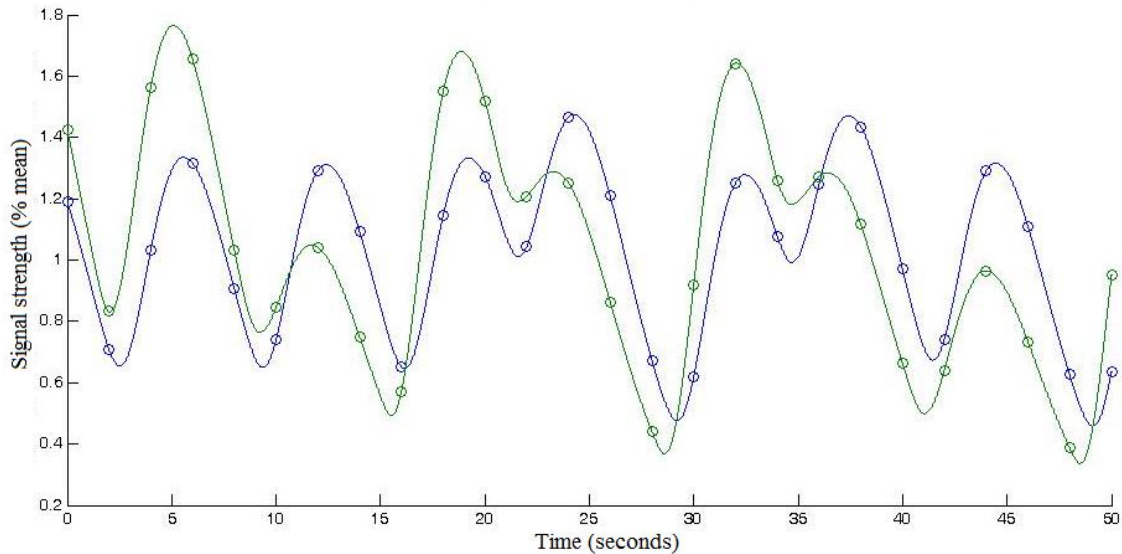
855 to describe the expected response pattern in the BOLD signal, for a given amount
 856 a neural activity. By convolving $HRF(t)$ with the long-form LFP templates
 857 ($\widehat{LFP}(t)$), we are able to generate predicted BOLD activity patterns that are directly
 858 comparable to the measured data.



859
 860 Figure 8. Excerpted BOLD predictions computed for two fields in Model 2: fAtn (blue) and
 861 go node (green). Same starting time point as in Figure 7 was used. Depicted is a sequence
 862 of seven trials at Load 4 with order Go-Nogo-Go-Nogo-Go-Nogo-Nogo.

863
 864 Note that time variable in $HRF(t)$ and $\widehat{LFP}(t)$ has different units, seconds
 865 (former) and milliseconds (latter). Also, note that we used a mapping of 1 model
 866 time-step to 1 ms in the experiment to simulate the details of each trial. Thus, care
 867 should be taken to bring these time units on the same scale, before the convolution
 868 $BOLD(t) = (HRF * \widehat{LFP})(t)$ is computed. Figure 8 shows two examples of BOLD
 869 predictions obtained as described above.

870 Next, we address the question of comparing model units for the numerically
871 generated BOLD signal to those derived from the fMRI data. We again take
872 guidance from the treatment of fMRI data: we normalize each predicted BOLD
873 signal by its average value over time across the entire
874



875
876 Figure 9. Excerpted normalized and downsampled BOLD predictions computed for two
877 fields in Model 2: fAtn (blue) and go node (green). Circles indicate the 2-second resolution
878 used to match the fMRI TR. The time range is the same as in Figure 8.

879
880 experiment-length time series. This takes us away from model-based units to an
881 abstract percentage scale relative to the mean.

882 Then we turn these normalized BOLD signal predictions into regressors for
883 the statistical analysis of the fMRI data. Care should be taken at this step, again,
884 given that the calculations require matching the sampling rate of the time series to
885 that of the data (down sampling to match the temporal resolution (TR) from the
886 fMRI data). Figure 9 shows the normalized BOLD signals resulting from those
887 shown in Figure 8, as well as the discrete sequence of points retained from the
888 numerically generated BOLD signal after down sampling.

889 Note that in the analysis of the GnG task, we decided to create split
890 regressors for Go and Nogo trials (see following section for details). To split the
891 trials, two long-form LFPs (again, for each subject and each component) were

892 created based on only Go or Nogo trial onsets instead of all trials together. The
893 proceeding steps from long-form LFP to regressor follow identically.

894 **7. Testing model-based predictions with GLM**

895 In the previous section, we generated a linking hypothesis that allows us to
896 specify a local-field potential for each field in a dynamic neural field model. We
897 also detailed the steps required to transform these LFPs into hemodynamic
898 predictions that are tailored to each individual participant. The next step is to
899 evaluate whether these individually-tailored hemodynamic predictions are, in fact,
900 *good* predictions relative to the fMRI data from each individual.

901 We used GLM to evaluate this question. In particular, we used the
902 individually-tailored hemodynamic predictions described above as regressors in a
903 GLM for each individual participant's fMRI data. This provides quantitative metrics
904 with which we can evaluate the model's goodness of fit. In particular, we examined
905 the following metrics from each individual GLM: (1) the number of voxels where
906 the model-based GLM captured a significant proportion of variance, and (2) the
907 average R^2 value across all significant voxels. Note that, because the R^2 values
908 were not normally distributed, we z-transformed the data. An average z-value was
909 calculated across the mask of voxels that were significant. The z-transformation
910 was then undone using $R = \text{atanh}(z)$, where z is the average z-value. Finally, the
911 R-value was adjusted using

$$912 \quad \text{adj}R = 1 - \frac{(1 - R)(N - 1)}{N - p - 1}$$

913 where N = number of time points across runs and $p = 1$.

914 Although the GLM approach gives us quantitative metrics, we need a way
915 to assess whether the fit of the model is any good. As Turner et al. discuss, the
916 optimal approach here would be to quantitatively compare the fit of the DNF model
917 relative to a competing model (Turner et al., 2016). For instance, in Buss et al.,
918 they compared hemodynamic predictions of the DNF model to hemodynamic
919 predictions of ACT-R (A. T. Buss et al., 2013). Here, we pursue an alternative
920 approach that was motivated by a recent model-based fMRI study of VWM. In that
921 study, we did not have a second cognitive model from which to generate competing

922 fMRI predictions. Instead, we compared the GLM-based fit of a DNF model to
923 Standard GLM fMRI analyses. This is useful because, at present, Standard GLM
924 fMRI analyses are the gold standard in the functional neuroimaging literature and
925 such analyses can be performed in all cases. Thus, we can treat the **Standard**
926 **GLM analysis** as a baseline and ask whether the **DNF-based GLM** quantitatively
927 outperforms this baseline.

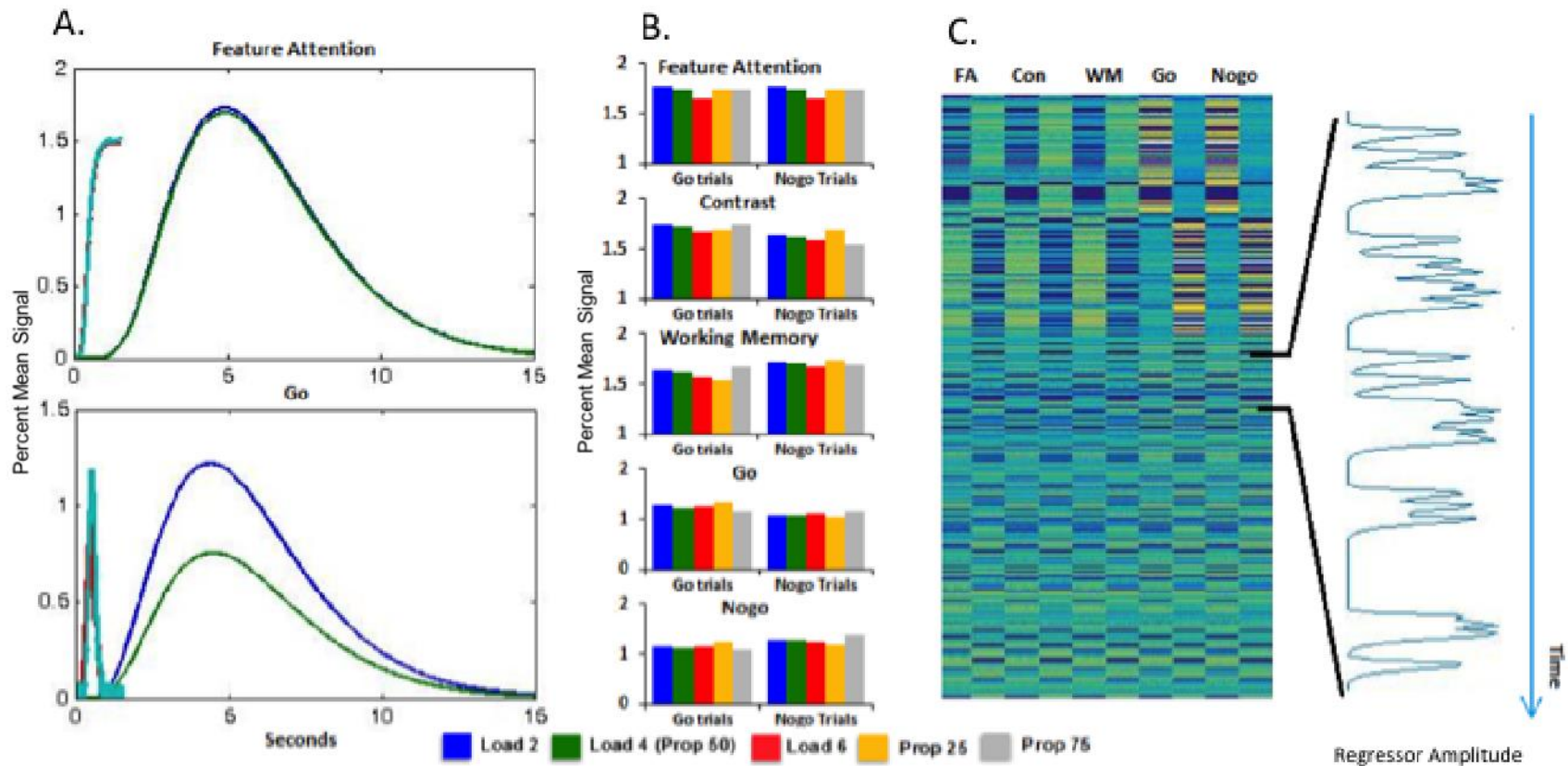
928 The next question is, of course, which metric to use. One option is to
929 analyze voxel counts; however, several studies have highlighted the limitations of
930 this approach (Bennett & Miller, 2010; Cohen & DuBois, 1999). An alternative is to
931 compare the mean R^2 values across models. The problem here is that the DNF-
932 based GLM might capture significant variance in some voxels, while the Standard
933 GLM analysis might capture significant variance in different voxels. The overall
934 mean R^2 value does not take this into effect. Thus, we used an alternative
935 approach: we created an intersection mask that defined voxels where the DNF-
936 based GLM and the Standard GLM analysis both captured a significant proportion
937 of variance and then statistically compared these intersection R^2 values. This
938 provides a direct head-to-head comparison of the two models in the same voxels,
939 asking which model does a better job fitting the brain data. Our objective was to
940 see whether we could tune the DNF model parameters such that it significantly
941 outperformed the Standard GLM analysis on this comparison metric.

942 We struggled with two final issues. First, the degrees of freedom of the DNF-
943 based GLM and Standard GLM analysis were not the same. The Standard GLM
944 analysis of data from Wijeakumar et al. (2015) had 10 regressors: 5 conditions
945 (Proportion 75%, Proportion 25%, Load 2, Load 4, Load 6) x 2 trial types (Go,
946 Nogo). By contrast, the DNF model had 7 regressors--one for each component
947 (vis, sAtn, fAtn, con, wm, go, nogo; see, for instance, Figure 9) – see section 6 for
948 the steps leading up to the creation of regressors from the DNF components.
949 Second, we discovered when running the DNF-based GLM that several regressors
950 were collinear which can make beta estimates unstable. This was not terribly
951 surprising: the most collinear fields were vis, sAtn, and fAtn, and all three fields
952 basically serve the same function in the GnG task.

953 To resolve both issues, we created a 10-regressor DNF-based GLM model
954 by (1) reducing the number of model components to the 5 least collinear fields
955 (fAtn, con, wm, go, nogo), and (2) including separate model-based regressor for
956 Go and Nogo trials.

957 Figure 10 illustrates the DNF-based GLM approach with numerical results
958 from Model 2. Figure 10A shows examples of HDRs and LFPs for Load 4 Go and
959 Nogo trials in the fAtn field and go node--the same fields used for illustration in
960 Figures 5-9. As above, differences in the HDR amplitude between Go and Nogo
961 trials are evident in the go node but not in the fAtn field. Maximum HDRs across
962 the five DNF components included in the GLM (fAtn, con, wm, go, nogo) and
963 across Load and Proportion manipulations are displayed in Figure 10B. These bars
964 reveal differences in the model-based predictions across components and
965 conditions. Note, for instance, that fAtn shows comparable hemodynamic
966 predictions across go and nogo trials, while the go and nogo nodes show different
967 patterns with, for instance, greater activation in the Prop25 condition on go trials,
968 and greater activation in the Prop75 condition on nogo trials. This reflects one of
969 the key hemodynamic patterns evident in the fMRI data: some brain areas showed
970 a strong response on infrequent trials, regardless of whether those trials required
971 inhibition (a nogo trial in the Prop75 condition) or not (a go trial in the Prop25
972 condition).

973 Figure 10C shows go and Nogo trial regressors for each component of the
974 model, constructed by inserting the condition-specific HDR at the onset of each
975 trial in the same order that was presented to each participant. An example predictor
976 for one participant – a regressor in the GLM model – is shown in the inset in Figure
977 10C. This time course was created by inserting the predicted hemodynamic time
978 course from the Nogo component (similar to those from Figure 10A) for each trial
979 type at the appropriate start time in the time series and then summing these
980 predictions. If there is a brain region involved in the generation of a Nogo decision,
981 the model predicts that this brain area should show the particular pattern of BOLD
982 changes over time shown in the inset. The GLM results can be used to statistically
983 evaluate such predictions.



984

985 Figure 10. Testing DNF model predictions with GLM (numerical results using Model 2): (A) Average HDR and LFP for Go (blue/cyan)
 986 and Nogo (green/red) Load 4 trials for the fAtn field and go node. (B) Predictions for five components of DNF model (fAtn, con, wm,
 987 go, nogo) across Load and Proportion manipulations; bars show signal change. (C) DNF regressors of a single subject and a sampling
 988 of the nogo node's time course (at right).

989 **8. Model evaluation: Individual-level GLMs**

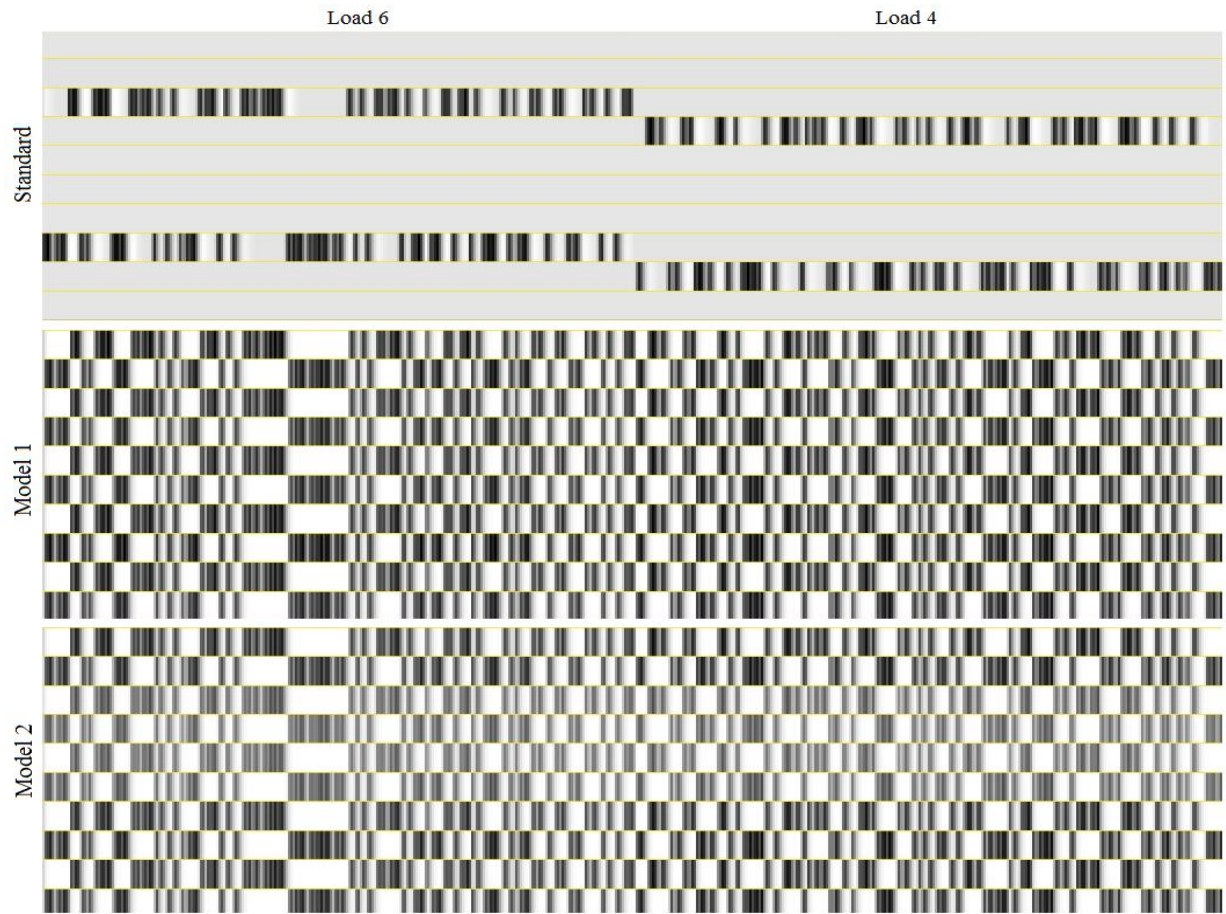
990 We ran 3 sets of GLM models (using `afni_proc` in AFNI) for each participant:
991 a 10-regressor DNF-based GLM for **Model 1**; a 10-regressor DNF-based GLM for
992 **Model 2**; and a 10-regressor **Standard GLM analysis**. All GLM analysis also
993 included regressors for motion and drifts in baseline. Figure 11 shows portions of
994 the 10 regressor design matrices from the three models we investigated. Note in
995 particular that the Standard GLM analysis employs a separate regressor for each
996 trial type and condition. In contrast, the DNF model-based method only separates
997 trials based on trial type (go and Nogo trials). For this reason, the model-based
998 method generates more constrained predictions because the relationship between
999 trial conditions (variations in Load and Proportion) is determined a priori and not
1000 allowed to vary independently as with the Standard GLM analysis method. As well,
1001 the model-based method employs different predictions for each model component,
1002 allowing us to identify effects indicative of specific functions.

1003 In each case, we report the total number of significant voxels and the mean
1004 R^2 value across those voxels (see below). We then intersected the images as per
1005 the model pairs and identified voxels that were significant for both Model 1 and the
1006 Standard GLM analysis, and voxels that were significant for both Model 2 and the
1007 Standard GLM analysis. Then, we calculated the mean intersection R^2 value for
1008 each model for each participant and compared these values using a paired-
1009 samples t-test.

1010 Overall voxel counts across models were the following: Model 1 = 3964
1011 voxels, Model 2 = 4762, Standard GLM analysis = 3978 voxels. Overall, both
1012 models were comparable but Model 2 captured significant variance in more voxels.
1013 The overall R^2 values were the following: Model 1 = 0.139, Model 2 = 0.135,
1014 Standard GLM analysis = 0.130, so both DNF models captured more variance,
1015 though neither represents a significant improvement relative to the Standard GLM
1016 analysis when we compare the average values computed across all voxels ($p=0.20$
1017 and $p=0.43$, respectively).

1018 The important metric in this evaluation between the DNF-based GLM and
1019 the Standard GLM analysis is the intersection R^2 values across model pairs. The

1020 intersection R^2 was 0.153 for Model 1 and 0.141 for the Standard GLM analysis
1021 across 1616 intersected voxels; Model 1 performed better than the Standard GLM
1022 analysis but this effect did not reach significance ($t(19) = 0.199$, $p=0.086$). On the
1023 other hand, the intersection R^2 was 0.150 for Model 2 and 0.131 for the Standard
1024 GLM analysis across 1507 intersected voxels, with Model 2 performing
1025 significantly better than the Standard GLM analysis ($t(19) = 0.427$, $p=.006$). When
1026 both DNF models were compared against each other, intersection R^2 values
1027 across 1615 intersected voxels were not significantly different, but Model 2
1028 performed quantitatively better than Model 1 (Model 1 = 0.148 and Model 2 =
1029 0.149, $t = 0.01$, $p=0.18$). In summary, Model 2 significantly outperforms the
1030 Standard GLM analysis and quantitatively performs better than Model 1. Thus, at
1031 the group level analysis, we only compared results between Model 2 and the
1032 Standard GLM analysis.
1033



1034
 1035 Figure 11. Excerpts from the 10-regressor design matrices for one subject from the three GLMs from the project. The excerpts are
 1036 taken from part of the Load 6 and Load 4 experimental blocks for the given subject. Note that differences exist in the model regressors
 1037 between components, but they are difficult to appreciate at this scale/resolution.

1038 **9. Model evaluation: Group-level GLMs**

1039 9.1 Overview of the approach

1040 The betamaps from the Standard GLM analysis were input into two 2-factor
1041 ANOVAs, a Load ANOVA and a Proportion ANOVA (run using *3dMVM*). The Load
1042 ANOVA consisted of Type and Load as factors and the Proportion ANOVA
1043 consisted of Type and Proportion as factors. The main effect and interaction maps
1044 from both sets of ANOVAs were thresholded and clustered based on family-wise
1045 corrections obtained from *3dClustSim* ($\alpha = .05$). The main effect of Type from the
1046 Proportion and Load ANOVAs were pooled together and called the 'Type main
1047 effect' image. The 'Other effects' image consisted of the pooled effects from the
1048 Load main effect, Proportion main effect, Load x Type interaction, and Proportion
1049 x Type interaction.

1050 The DNF-based GLM (Model 2 only) also yielded betamaps for each of the
1051 ten regressors. These betamaps were input into an ANOVA with regressor as the
1052 only factor. The main effect of regressor obtained from this ANOVA was corrected
1053 for family wise errors using *3dClustSim* as described above. A one-sample t-test
1054 was conducted within the spatial constraints of this clustered main effect image to
1055 ascertain the contribution of each regressor to the main effect. These t-test results
1056 for each regressor were corrected for family wise errors again, identifying which
1057 model components were significant predictors for each voxel. At this point, we
1058 collapsed effects across trial type for each regressor. For instance, voxels that
1059 showed an effect of the wm field for Go trials and/or for Nogo trials were pooled
1060 together as wm areas. Consequently, the final image consisted of voxels that
1061 showed unique and combined contributions from five fields in the DNF model --
1062 fAtn, con, wm, go node and nogo node. This map was intersected with the Type
1063 effect and Other Effects maps from the Standard GLM analysis to establish
1064 whether the two GLM analyses identified similar brain regions and whether effects
1065 in each cluster were comparable.

1066 It is important to note that the DNF-based approach not only identifies *where*
1067 the brain responded in a way predicted by the model, but also *which function(s)*
1068 operates within that brain region. Thus, in the section that follows, we examine the

1069 functional networks identified by the DNF model and then compare the spatial
1070 overlap between the DNF-based GLM and the Standard GLM analysis.

1071 9.2 Group-level Results

1072 Figure 12 shows those DNF model predictors that produced statistically
1073 significant clusters within the brain regions showing a main effect of component.
1074 Overall, the DNF-based GLM revealed patterns of activation consistent with the
1075 model-based predictions in cortical and sub-cortical networks of the brain that
1076 included the cerebellum, putamen, insula, caudate, supplementary motor area
1077 (SMA), as well as parts of the occipital cortex and the cingulate cortex.

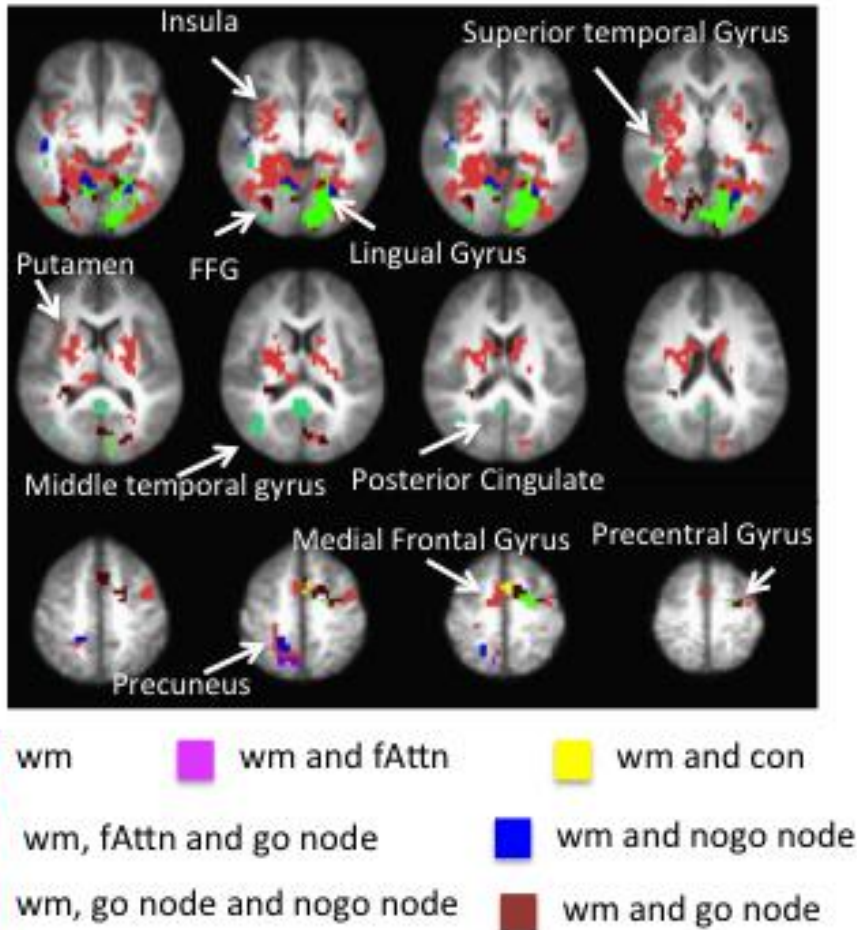
1078 Unique contributions from the wm field recruited the largest numbers of
1079 regions (accounting for 1738 voxels). Critically, key parts of the insular-thalamic-
1080 putamen network were assigned to a working memory function, consistent with
1081 claims by Hampshire and colleagues (Erika-Florence et al., 2014) that working
1082 memory and attention processes may underlie response selection. Clusters that
1083 showed combined effects from more than one component accounted for 965
1084 voxels. Importantly, all of these voxels included a common wm component.
1085 Looking at the model predictions from Figure 10B, two patterns likely explain the
1086 predominance of the wm field predictions: (1) there is a reduction in wm activation
1087 as Load was increased, and (2) there is a larger modulation of wm activation
1088 across the Proportion manipulation on Go trials relative to Nogo trials. As
1089 discussed in Wijekumar et al. (2015), both patterns were pervasive in the fMRI
1090 data.

1091 The DNF-based GLM approach also identified regions that laid outside of
1092 the network obtained from the Standard GLM analyses approach. The wm field
1093 recruited parts of the left fusiform gyrus, left cuneus and left superior temporal
1094 gyrus. The lingual gyrus and fusiform gyrus also reflected neural predictions of a
1095 combination of the wm, go, and nogo fields. This is consistent with previous
1096 findings suggesting that the lingual gyrus plays a role in visual memory as well as
1097 visual classification decisions (Mechelli, Humphreys, Mayall, Olson, & Price,
1098 2000). Our results also assign the same functional role to the fusiform gyrus which
1099 is functionally connected to the lingual gyrus and plays a central role in visual

1100 processing and visual comparison (Mechelli et al., 2000). Another result is the
1101 recruitment of parts of the left middle frontal gyrus (not shown) by the wm field and
1102 a combination of the wm field and go and nogo nodes (Johnson, Hollingworth, &
1103 Luck, 2008; Johnson, Spencer, Luck, & Schöner, 2009; Simmering, Peterson,
1104 Darling, & Spencer, 2008). The wm field plays a very important role of maintaining
1105 memory traces in the DNF model of VWM in adulthood and development.
1106 Furthermore, the middle frontal gyrus has been implicated to be involved in
1107 maintenance of goals and abstract representations during VWM processing (Aoki
1108 et al., 2011; Barbey, Koenigs, & Grafman, 2013; Haxby, Petit, Ungerleider, &
1109 Courtney, 2000; Jonides et al., 1998; Munk et al., 2002; Pessoa, Gutierrez,
1110 Bandettini, & Ungerleider, 2002; Pessoa & Ungerleider, 2004).

1111 The next question we examined was how these results from the DNF-based
1112 GLM overlapped with results from the Standard GLM analysis. Table 1 shows
1113 voxel counts for common and unique effects between these GLM results. Figure
1114 13 shows the spatial distribution of these clusters for the unique and common
1115 effects. The Type main effect from the Standard GLM analysis overlapped with
1116 534 voxels that were also significant in the DNF-based GLM (Figure 13; yellow).
1117 In addition, the 'Other effects' from the Standard GLM analysis overlapped with
1118 116 voxels that were also significant in the DNF-based GLM (shown in brown in
1119 Figure 13). We focus on these overlapping effects below because they provide a
1120 way to evaluate our model-based fMRI results relative to findings discussed in
1121 Wijekumar et al. (2015).

1122



1123

1124 Figure 12. Functional maps generated by DNF model. Colored regions represent cortical
 1125 areas where a main effect of component was present.

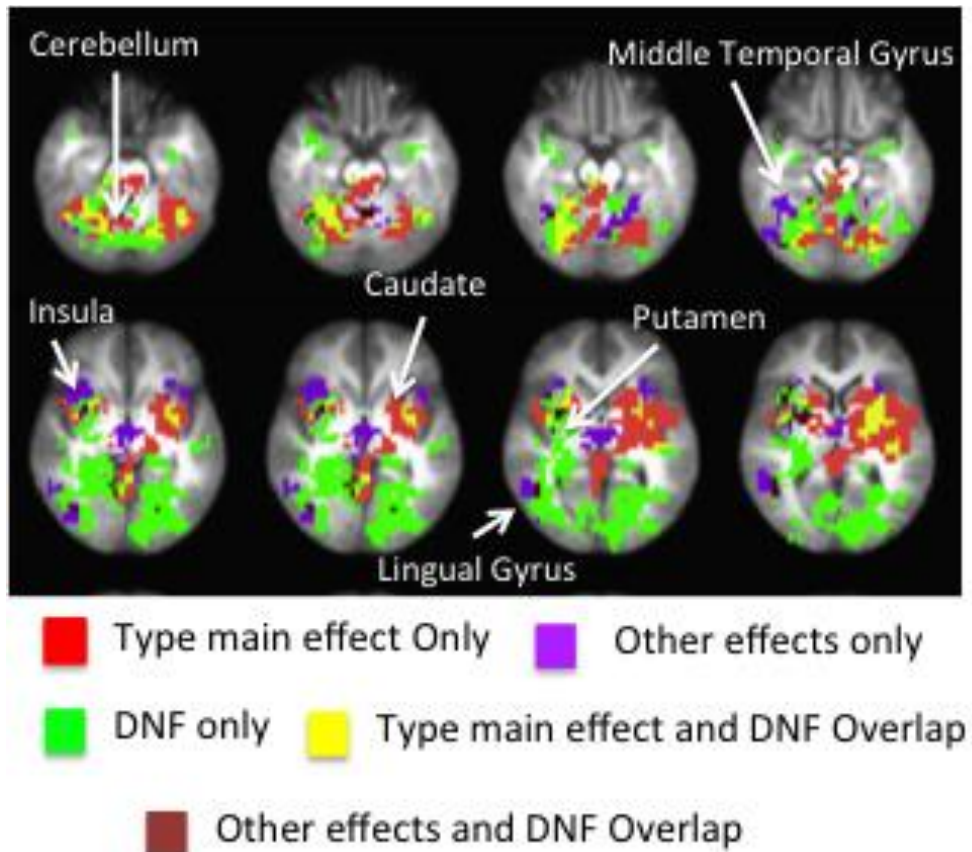
1126

1127 Tables 2 and 3 show clusters that overlapped between the DNF-based GLM
 1128 and the Type main effect and Other effects respectively. For each overlapping
 1129 cluster, we identify the fields that were significant in the DNF-based GLM.

1130 Table 1. Voxel count of unique and common effects between the DNF-based GLM and
 1131 Standard GLM analysis activation maps.

	Voxel Count
Type Main Effect only	2610
Other Effects only	414
DNF Components only	2053
DNF Components and Type Main Effects	494
DNF Components and Other Effects	97

1132



1133

1134 Figure 13. Overlap between DNF and the Standard GLM analysis.

1135

1136

1137

1138

1139

1140

1141

1142

1143

1144

1145

1146

1147

1148

Critically, there was overlap between the areas recruited by the wm field and the Type main effect in parts of the insular-thalamic-putamen network. As noted above, this is consistent with claims by Hampshire and colleagues that working memory plays a central role in response selection via activation of anterior insular and frontal operculum network (Erika-Florence et al., 2014; Hampshire & Sharp, 2015). Overlap between combinations of the wm field and other components and the Type main effect was also observed in parts of the cerebellum and SMA. It is interesting that activation elicited by the DNF components seemed more localized as compared to the activation from the Type main effect (see yellow regions embedded in red regions in Figure 13). This is an encouraging sign for future work, suggesting that the DNF model might identify functional networks that are more precisely localized than what is typically revealed by Standard GLM analyses.

1149 The Other effects activation maps contained the effects of Proportion and
1150 Load and interactions of these two manipulations with Type of trial. Once again,
1151 the greatest degree of overlap was with the wm field, including portions of the
1152 cerebellar regions and also the insula and putamen. In our previous work, this
1153 insular network has been implicated in detecting salient or infrequent events
1154 (Wijeakumar et al., 2015). In the model, the wm field is responsible for associating
1155 and retrieving the appropriate SR mappings to both frequent or non-salient and as
1156 well as infrequent, salient events. As noted above, the wm field showed two key
1157 effects that were pervasive in the Standard GLM analysis results: a reduction in
1158 activation over Load and a larger modulation of wm activation across the
1159 Proportion manipulation on Go trials relative to Nogo trials. This likely explains the
1160 overlap between predictions from the wm field and the Other effects.
1161

1162 Table 2. Spatial overlap between DNF model and the Type main effect from the Standard
 1163 GLM analysis.

Components	Intersected with	Region	Hemi	Volume (mm ³)	Center of Mass		
					x	y	z
WM	Type ME	Putamen	L	4502	22.6	3.1	10.8
	Type ME	Cerebellum	L	1458	2.6	66.5	-30.4
	Type ME	Cerebellum	R	1158	-15.6	47.7	-33.8
	Type ME	Caudate Nucleus	R	943	-21.2	7.8	18.3
	Type ME	Superior Temporal Gyrus	L	858	37.8	24.4	6.8
	Type ME	Putamen	R	686	-23.2	-9.1	4.5
	Type ME	Cerebellum	L	514	17.5	56.1	-40.2
	Type ME	Cerebellum	R	429	-28.0	64.0	-14.2
	Type ME	Cerebellum	R	386	-34.8	51.2	-25.8
	Type ME	Cerebellum	R	386	-17.3	53.9	-22.7
	Type ME	Thalamus	R	343	-9.2	23.3	14.4
	Type ME	Cingulate Gyrus	R	343	6.1	21.1	33.6
	Type ME	SMA	R	257	-3.5	5.1	54.9
	Type ME	Cerebellum	L	214	25.6	72.4	-11.0
	Type ME	Cerebellum	L	172	24.5	51.8	-46.0
	Type ME	Insula	R	172	-36.8	1.9	3.0
	Type ME	Cerebellum	-	172	0.0	44.8	-0.5
	Type ME	Cerebellum	R	129	-30.9	43.0	-33.2
	Type ME	Cerebellum	R	129	-20.4	60.5	-12.2
	Type ME	Caudate Nucleus	R	129	-11.1	-3.7	20.5
	Type ME	Posterior Cingulate Cortex	L	129	5.2	27.8	26.3
	Type ME	Cerebellum	L	86	10.5	64.0	-35.5
	Type ME	Cerebellum	R	86	-8.8	43.0	-5.8
Type ME	Cerebellum	R	86	-3.5	53.5	-7.5	
Type ME	Thalamus	R	86	-19.2	6.2	3.0	
WM and fAtn	Type ME	Cerebellum	L	129	7.6	69.8	-11.0
WM, Go node and Nogo node	Type ME	Fusiform Gyrus	L	86	24.5	74.5	-7.5
	Type ME	SMA	L	86	12.2	6.2	55.5
WM and Con	Type ME	SMA	L	86	1.8	1.0	53.8
WM and Go node	Type ME	Cerebellum	L	514	35.0	50.0	-21.5
	Type ME	Putamen	L	514	22.8	14.1	8.2
	Type ME	Putamen	L	429	32.2	4.8	3.0
	Type ME	Cerebellum	R	257	-24.5	71.0	-13.3
	Type ME	Cerebellum	R	129	-41.4	51.2	-21.5
WM and Nogo node	Type ME	Cerebellum	R	2187	-25.6	48.9	-17.1
	Type ME	Cerebellum	L	686	17.7	59.6	-22.2
	Type ME	Cerebellum	R	557	-7.7	62.4	-30.9
	Type ME	Cerebellum	R	514	-9.3	25.5	-19.5
	Type ME	Cerebellum	R	343	-16.6	53.9	-42.1
	Type ME	Cerebellum	R	214	-13.7	50.0	-6.8
	Type ME	Cerebellum	L	172	41.1	51.8	-18.9
	Type ME	Cerebellum	L	172	24.5	58.8	-11.0
	Type ME	Cerebellum	R	129	-18.1	34.8	-21.5
	Type ME	Cerebellum	L	86	-12.2	64.0	-19.8

1164

1165 Table 3. Spatial overlap between the DNF model and the Other effects from the Standard
 1166 GLM analysis.

Components	Intersected with	Region	Hemi	Volume (mm ³)	Center of Mass		
					x	y	z
WM	Other Effects	Inferior Occipital Gyrus	R	943	-39.8	69.1	-6.2
	Other Effects	Cerebellum	R	557	-18.4	54	-28
	Other Effects	Putamen	R	557	-26	-0.3	4.9
	Other Effects	Middle Temporal Gyrus	R	386	-44.1	51.2	6.1
	Other Effects	Cerebellum	L	300	7.8	50	-8.5
	Other Effects	Cerebellum	L	257	1.8	48.2	-18
	Other Effects	Insula	R	172	-36.8	-12.1	6.5
	Other Effects	Fusiform Gyrus	R	129	-35.6	50	-15.7
	Other Effects	Putamen	R	86	-28	-9.5	-4
	Other Effects	Insula	R	86	-33.2	-18.2	6.5
	Other Effects	Caudate Nucleus	L	86	8.8	4.5	15.2
WM, fAtn and Go node	Other Effects	Inferior Occipital Gyrus	R	86	-38.5	74.5	-4
WM, Go node and Nogo node	Other Effects	Lingual Gyrus	L	172	13.1	64	-4
	Other Effects	Cerebellum	L	86	17.5	67.5	-7.5
WM and Go node	Other Effects	Fusiform Gyrus	R	86	-26.2	65.8	-4
WM and Nogo node	Other Effects	Cerebellum	R	86	-14	64	-25
	Other Effects	Cerebellum	R	86	-8.8	55.2	-0.5

1167

1168

1169 **10. General Discussion**

1170 The objective of the current paper was to formalize an integrative cognitive
1171 neuroscience approach using DFT. To this effect, we adopted a tutorial-style
1172 approach wherein we first introduced DFT and its applications to readers who
1173 might be less familiar with this modeling approach. Then, we used data from a
1174 response selection paradigm as an exemplar case study to explain the steps and
1175 rationale involved in building DNF models that could capture behavioral and neural
1176 data and the challenges in bridging brain and behavior using these methods. The
1177 central goal of this approach was to generate hemodynamic predictions from DNF
1178 models and evaluate these predictions at the individual and group levels using
1179 GLM by making comparisons to Standard GLM analyses.

1180 Two DNF models captured behavioral data from the task reasonably well;
1181 however, only one of the DNF models outperformed the Standard GLM analysis
1182 when comparing adjusted R^2 values within the same regions of the brain.
1183 Interestingly, this model architecture was developed by tuning the first model
1184 parameters to capture competitive neural interactions first and then simultaneously
1185 capturing behavioral data as well. This suggests that iterative modeling using this
1186 approach might be most effective. Model 2 was then advanced to the group level
1187 analyses to look at spatial distributions of DNF components and how these
1188 distributions overlapped with effects observed in the Standard GLM analysis from
1189 our previous work.

1190 The DNF model engaged a large cortico-sub-cortical network that included
1191 parts of the cerebellum, SMA, insula, putamen, thalamus, caudate and parts of the
1192 occipital cortex. In particular, unique contributions from the wm field accounted
1193 most of spatial distributions. The rest of the contributions were from a combination
1194 of effects between the wm field and other components in the DNF model. This
1195 finding is in line with Hampshire and colleagues who argue that response selection
1196 and inhibition is a property of spatially distributed functional networks that support
1197 a general class of working memory and attentional processes (Erika-Florence et
1198 al., 2014).

1199 These spatial distributions also overlapped with effects from the Standard
1200 GLM analysis. Findings from the Cisek lab might provide some evidence that are
1201 in line with our findings on the recruitment of a host of cortical and sub-cortical
1202 regions by the wm field that overlapped with areas showing a difference between
1203 Go and Nogo responses in the Standard GLM analysis (Cisek, 2012). These
1204 authors presented evidence that action selection emerges through a distributed
1205 consensus across many levels of representation, which in the current case would
1206 represent multiple SR mappings. According to this theory, cortical and subcortical
1207 regions compete through inhibitory interactions when individuals are faced with
1208 multiple potential actions. So, it is possible that the BOLD signal reduction reported
1209 in our previous work is related to the inhibitory competition between the Go and
1210 Nogo responses.

1211 The wm field also engaged regions in the occipital cortex, an insular
1212 ‘salience’ network, and the cerebellum. Collectively taken, we suggest that wm
1213 field is involved in processing visual information from the stimuli, to associating and
1214 retrieving the appropriate SR mappings to both frequent or non-salient and as well
1215 as salient events, before activating the motor planning and execution centers of
1216 the brain. These findings show a departure of our DNF model from typical
1217 integrative modeling approaches, as emphasized by Turner and colleagues
1218 (Turner et al., 2016). As these researchers underline, integrative models require a
1219 strong commitment to both the underlying cognitive process and where this
1220 process is executed in the brain. The DNF model does not fall into this category.
1221 The DNF model does show a strong commitment to specifying the cognitive and
1222 neural processes that underlie the behaviors in questions; however, our approach
1223 remains open to where in the brain these neural dynamics live. This is an important
1224 observation – remember, neurons do not always act like modules. Neurons can
1225 switch their allegiance, thus coding for multiple dimensions. So allowing for
1226 flexibility in the integrative modeling approach may be beneficial when mapping
1227 theories to cognitive processes in the brain. In the next section, we critically
1228 evaluate this modeling approach with an eye towards future efforts to optimize
1229 model performance and further DFT applications.

1230 10.1 Evaluating the model-based approach

1231 This tutorial has meticulously walked through explaining the background to
1232 DFT, previous applications, the rationale for developing DNF models, construction
1233 of the components of the fields of DNF models, and comparing quantitative fits to
1234 the behavioral and neural data to Standard GLM analyses. This raised several
1235 issues we summarize here in our efforts to formalize an integrative cognitive
1236 neuroscience approach.

1237 *Choosing parameters for DNF models:* We obtained reasonable behavioral fits for
1238 both DNF models using parameters grounded by previous work (Erlhagen &
1239 Schöner, 2002) and our experience with learning dynamics. That said, it is possible
1240 that different sets of parameters could provide similar quantitative behavioral fits.
1241 Future work will be needed to explore a broader range of parameters, asking two
1242 key questions: (1) are there parameters that provide a better fit to the behavioral
1243 and neural data, and (2) do we see the same qualitative behavioral and neural
1244 outcomes from the model across a range of parameters, without dramatic
1245 violations of the behavioral and neural patterns. The former question examines the
1246 goodness-of-fit of the model; the latter question probes the generality of the model.
1247 We think an iterative approach to model exploration would be most fruitful here,
1248 stressing the important constraints gained by modeling two data sets
1249 simultaneously from a single neural process model.

1250 *Constraining the model:* Despite not testing a multitude of parameters, there are
1251 still many points in this modeling approach where constraints have been placed.
1252 To begin, the architecture was heavily constrained by using components that have
1253 a history in explaining working memory processes (Johnson, Spencer, & Schöner,
1254 2008; Johnson et al., 2009; Simmering & Spencer, 2007). This was done to place
1255 emphasis on the generalization of these components across different executive
1256 functions. Next, we constrained the model to account for both behavioral and
1257 neural data -- the key strength of adopting an integrative cognitive neuroscience
1258 approach. Concretely, constraints here come from the direct mapping of neural
1259 activation patterns in the model to LFPs to simulated BOLD data. Finally, in future

1260 work, constraints can also be applied when mapping from one model to the next
1261 with a goal to integrate across DNF architectures.

1262 *Model Complexity* When contrasted with other cognitive models, DNF models
1263 seem rather complex. They are composed of several fields and parameters that
1264 require fine-tuning to generate good fits to both behavioral and neural data.
1265 However, this added level of complexity is to be expected if one tries to bridge non-
1266 linear patterns of brain activity and macroscopic behavioral responses. We
1267 contend that bridging brain and behavior requires models that take into account
1268 how neural systems actually work. DFT does this by faithfully capturing many
1269 known properties of neural population dynamics and how neural populations are
1270 recurrently connected across multiple cortical fields to give rise to complex
1271 behaviors (Bastian, Riehle, Erlhagen, & Schöner, 1998; Bastian et al., 2003;
1272 Erlhagen et al., 1999).

1273 That said, it is also important to note that DFT does not consider other
1274 known aspects of neural function such as the details of neurotransmitter action,
1275 the biophysical properties of individual neurons, and so on (Garagnani,
1276 Wennekers, & Pulvermüller, 2008; Markram et al., 2015). In this sense, DFT
1277 provides a limited view of neural function. To the extent that these details matter,
1278 even more complex biophysical models will be required if we want to bridge brain
1279 and behavior. Our claim, however, is that many of these low-level biophysical
1280 details are not necessary when capturing fMRI data because fMRI provides on a
1281 low-pass filter on neural activity. Future work will be needed to evaluate this
1282 conjecture. Critically, however, the approach described here facilitates that work
1283 by providing a formal method to test whether neural population dynamics are
1284 sufficient to capture the details inherent in fMRI.

1285 *Exploratory versus confirmatory modeling approaches:* Turner et al. argue that
1286 integrative models are confirmatory by nature because fits to brain networks and
1287 behavioral patterns are constrained. We agree with this outlook (Turner et al.,
1288 2016). However, in the current case study, there is also an exploratory component.
1289 For instance, one of our central questions here was exploratory in nature: can
1290 components from previous working memory models capture brain and behavioral

1291 patterns in response selection? Once we have a model that does this, we can
1292 move into the confirmatory phase. A refined approach at this stage would be to
1293 design conditions in the task that de-correlate the fields of the DNF model. For
1294 instance, if we find that decreasing the proportion of go trials resulted in different
1295 LFP patterns in the *wm* field as compared to the *go* node, then a range of
1296 proportion of trials can be tested to determine the point at which collinearity
1297 between those two regressors would be at the lowest, whilst still preserving the
1298 integrity of the DNF model. Further, one could test the efficiency of multiple design
1299 matrices constructed from such regressors. After this confirmatory phase, one
1300 could optimally test the model across a range of scenarios. Indeed, the ideal
1301 scenario is one in which the confirmatory phase enables contrasts with other
1302 theories that make different predictions for both brain and behavior.

1303 We note, however, that doing this requires having comparable theoretical
1304 approaches such as two integrative cognitive neuroscience models. At present,
1305 this is difficult given that there are relatively few integrative approaches (but see,
1306 Buss et al., 2013). One alternative is to contrast two different models from the
1307 same theoretical framework. We did a variant of this in the current study,
1308 contrasting Model 1 with Model 2. A more conceptually intriguing variant of this
1309 approach would be to contrast two different dynamic field architectures (rather than
1310 testing the same architecture under different parameter settings). When contrasted
1311 at the levels of both brain and behavior, this might enable one to eliminate
1312 candidate models based on the fit to data.

1313 *Difficulty of implementation:* Developing a dynamic field model and fitting the
1314 model to data is a complex enterprise. However, the recent book from the DFT
1315 group unpacks this complexity, providing the background to DFT including the
1316 underlying rationale. The book also offers multiple examples of implemented
1317 models that can help foster the development of new models. Further, the
1318 COSIVINA simulation environment allows researchers to build entire DF models
1319 using a few lines of code making implementation easy. We note that we have
1320 added a neuroimaging toolbox to this framework; thus, creating the LFPs
1321 described herein is quite easy (see www.dynamicfieldtheory.org/software/).

1322 *Uncovering the 'ground truth' amongst models:* An important issue to address in
1323 future work would be the nature of spatial neural patterns in the cortex that are
1324 revealed by the DNF-based approach relative to Standard GLM analyses. Most
1325 critically, when the two approaches disagree, which approach reveals the 'ground
1326 truth'? One interesting avenue to explore this question would be to carefully
1327 introduce different types of synthetic data into an fMRI dataset. For instance, one
1328 could effectively insert neural patterns consistent with the DNF model, inconsistent
1329 with the model, or unbiased to either approach. One could then use Standard GLM
1330 analysis and DNF approaches to fish out these activation patterns. In this case,
1331 one knows the 'ground truth' and it is easier to evaluate which method outperforms
1332 the other. Then one could explore the overlap (or lack thereof) across spatial
1333 distributions between approaches to better understand the discrepancies.

1334 Although future work in this direction will be needed, we note that compared
1335 to Standard GLM analyses, DNF models are grounded in a formal theory that
1336 specifies how neural populations dynamics give rise to behavioral patterns. In this
1337 sense, the fact that the DNF-based GLM reported here outperformed the Standard
1338 GLM analysis on key quantitative metrics is important. Nevertheless, we recognize
1339 that there is often an inherent mistrust with formal models and empirically-oriented
1340 researchers will likely gravitate toward Standard GLM analyses to provide the
1341 'ground truth'. This is certainly a reasonable approach until the DNF-based
1342 integrative cognitive neuroscience approach proves its worth across multiple
1343 projects.

1344

1345 **Acknowledgments**

1346 This material is based upon work supported by the National Science Foundation
1347 under Grant Number BCS-1029082 (awarded to JPS and RC).

References

- 1349 Amari, S. (1977). Dynamics of Pattern Formation in Lateral-Inhibition Type
 1350 Neural Fields*. *Biological Cybernetics*, 27(2), 77–87.
 1351 <http://doi.org/10.1007/BF00337259>
- 1352 Anderson, J. R. (2012). Tracking problem solving by multivariate pattern analysis
 1353 and Hidden Markov Model algorithms. *Neuropsychologia*, 50(4), 487–498.
 1354 <http://doi.org/10.1016/j.neuropsychologia.2011.07.025>
- 1355 Anderson, J. R., Matessa, M., & Lebiere, C. (1997). ACT-R: A Theory of Higher
 1356 Level Cognition and its Relation to Visual Attention. *Human-Computer*
 1357 *Interaction*. http://doi.org/10.1207/s15327051hci1204_5
- 1358 Aoki, R., Sato, H., Katura, T., Utsugi, K., Koizumi, H., Matsuda, R., & Maki, A.
 1359 (2011). Relationship of negative mood with prefrontal cortex activity during
 1360 working memory tasks: An optical topography study. *Neuroscience*
 1361 *Research*, 70(2), 189–196. <http://doi.org/10.1016/j.neures.2011.02.011>
- 1362 Aron, A. R., Robbins, T. W., & Poldrack, R. A. (2014). Inhibition and the right
 1363 inferior frontal cortex: One decade on. *Trends in Cognitive Sciences*.
 1364 <http://doi.org/10.1016/j.tics.2013.12.003>
- 1365 Barbey, A. K., Koenigs, M., & Grafman, J. (2013). Dorsolateral prefrontal
 1366 contributions to human working memory. *Cortex*, 49(5), 1195–1205.
 1367 <http://doi.org/10.1016/j.cortex.2012.05.022>
- 1368 Bastian, A., Riehle, A., Erhagen, W., & Schöner, G. (1998). Prior information
 1369 preshapes the population representation of movement direction in motor
 1370 cortex. *NeuroReport*, 9, 315–319.
- 1371 Bastian, A., Riehle, A., Erhagen, W., & Schöner, G. (1998). Prior information
 1372 preshapes the population representation of movement direction in motor
 1373 cortex. *Neuroreport*, 9(2), 315–9.
- 1374 Bastian, A., Schöner, G., & Riehle, A. (2003). Preshaping and continuous
 1375 evolution of motor cortical representations during movement preparation.
 1376 *European Journal of Neuroscience*, 18, 2047–2058.
- 1377 Bennett, C. M., & Miller, M. B. (2010). How reliable are the results from functional
 1378 magnetic resonance imaging? *Annals of the New York Academy of*
 1379 *Sciences*, 1191(1), 133–155. [http://doi.org/10.1111/j.1749-](http://doi.org/10.1111/j.1749-6632.2010.05446.x)
 1380 [6632.2010.05446.x](http://doi.org/10.1111/j.1749-6632.2010.05446.x)
- 1381 Bicho, E., & Schöner, G. (1997). The dynamic approach to autonomous robotics
 1382 demonstrated on a low-level vehicle platform. *Robotics and Autonomous*
 1383 *Systems*, 21(1), 23–35. [http://doi.org/10.1016/S0921-8890\(97\)00004-3](http://doi.org/10.1016/S0921-8890(97)00004-3)
- 1384 Borst, J. P., & Anderson, J. R. (2013). Using model-based functional MRI to
 1385 locate working memory updates and declarative memory retrievals in the
 1386 fronto-parietal network. *Proceedings of the National Academy of Sciences of*
 1387 *the United States of America*, 110(5), 1628–33.
 1388 <http://doi.org/10.1073/pnas.1221572110>
- 1389 Borst, J. P., Nijboer, M., Taatgen, N. A., Van Rijn, H., & Anderson, J. R. (2015).
 1390 Using data-driven model-brain mappings to constrain formal models of
 1391 cognition. *PLoS ONE*, 10(3). <http://doi.org/10.1371/journal.pone.0119673>
- 1392 Boucher, L., Palmeri, T. J., Logan, G. D., & Schall, J. D. (2007). Inhibitory control
 1393 in mind and brain: an interactive race model of countermanding saccades.

1394 *Psychological Review*, 114(2), 376–397. <http://doi.org/10.1037/0033->
1395 295X.114.2.376

1396 Bressloff, N. W. (2001). Three-dimensional pulsatile flow through asymmetrically
1397 and symmetrically constricted vessels. In *American Society of Mechanical*
1398 *Engineers, Bioengineering Division (Publication) BED* (Vol. 50, pp. 525–
1399 526).

1400 Buss, A., & Spencer, J. P. (2008). The emergence of rule-use: A dynamic neural
1401 field model of the DCCS. Retrieved from
1402 csjarchive.cogsci.rpi.edu/Proceedings/2008/pdfs/p463.pdf

1403 Buss, A. T., & Spencer, J. P. (2014). The emergent executive: A dynamic field
1404 theory of the development of executive function. *Monographs of the Society*
1405 *for Research in Child Development*, 79(2), 1–132.

1406 Buss, A. T., Wifall, T., Hazeltine, E., & Spencer, J. P. (2013). Integrating the
1407 behavioral and neural dynamics of response selection in a dual-task
1408 paradigm: A dynamic neural field model of Dux et al. (2009). *Journal of*
1409 *Cognitive Neuroscience*, 26, 334–351.

1410 Christopoulos, V., Bonaiuto, J., & Andersen, R. A. (2015). A Biologically
1411 Plausible Computational Theory for Value Integration and Action Selection in
1412 Decisions with Competing Alternatives. *PLoS Computational Biology*, 11(3).
1413 <http://doi.org/10.1371/journal.pcbi.1004104>

1414 Cisek, P. (2012). Making decisions through a distributed consensus. *Current*
1415 *Opinion in Neurobiology*. <http://doi.org/10.1016/j.conb.2012.05.007>

1416 Cohen, M. S., & DuBois, R. M. (1999). Stability, repeatability, and the expression
1417 of signal magnitude in functional magnetic resonance imaging. *Journal of*
1418 *Magnetic Resonance Imaging*, 10(1), 33–40.
1419 [http://doi.org/10.1002/\(SICI\)1522-2586\(199907\)10:1<33::AID-](http://doi.org/10.1002/(SICI)1522-2586(199907)10:1<33::AID-)
1420 [JMRI5>3.0.CO;2-N](http://doi.org/10.1002/(SICI)1522-2586(199907)10:1<33::AID-JMRI5>3.0.CO;2-N)

1421 Coombes, S., & Owen, M. R. (2005). Bumps, breathers, and waves in a neural
1422 network with spike frequency adaptation. *Physical Review Letters*, 94(14).
1423 <http://doi.org/10.1103/PhysRevLett.94.148102>

1424 Curtu, R., & Ermentrout, B. (2001). Oscillations in a refractory neural net. *Journal*
1425 *of Mathematical Biology*, 43(1), 81–100.
1426 <http://doi.org/10.1007/s002850100089>

1427 Davis, T., Love, B. C. B., & Preston, A. R. A. (2012). Striatal and hippocampal
1428 entropy and recognition signals in category learning: simultaneous
1429 processes revealed by model-based fMRI. *Journal of Experimental*
1430 *Psychology. Learning, Memory, and Cognition*, 38(4), 821–39.
1431 <http://doi.org/10.1037/a0027865>

1432 Deco, G., Rolls, E. T., & Horwitz, B. (2004). “What” and “where” in visual working
1433 memory: a computational neurodynamical perspective for integrating FMRI
1434 and single-neuron data. *Journal of Cognitive Neuroscience*, 16(4), 683–701.
1435 <http://doi.org/10.1162/089892904323057380>

1436 Dux, P. E., Tombu, M. N., Harrison, S., Rogers, B. P., Tong, F., & Marois, R.
1437 (2009). Training improves multitasking performance by increasing the speed
1438 of information processing in human prefrontal cortex. *Neuron*, 63(1), 127–38.
1439 <http://doi.org/10.1016/j.neuron.2009.06.005>

- 1440 Erika-Florence, M., Leech, R., & Hampshire, A. (2014). A functional network
 1441 perspective on response inhibition and attentional control. *Nat Commun*,
 1442 5(May), 4073. <http://doi.org/10.1038/ncomms5073>
- 1443 Erlhagen, W., Bastian, A., Jancke, D., Riehle, A., & Schöner, G. (1999). The
 1444 distribution of neuronal population activation (DPA) as a tool to study
 1445 interaction and integration in cortical representations. *Journal of*
 1446 *Neuroscience Methods*, 94, 53–66.
- 1447 Erlhagen, W., & Schöner, G. (2002). Dynamic field theory of movement
 1448 preparation. *Psychological Review*, 109, 545–572.
- 1449 Ermentrout, B. (1998). Neural networks as spatio-temporal pattern-forming
 1450 systems. *Reports on Progress in Physics*, 61(4), 353–430.
 1451 <http://doi.org/10.1088/0034-4885/61/4/002>
- 1452 Ermentrout, B., & Kleinfeld, D. (2001). Traveling Electrical Waves in Cortex.
 1453 *Neuron*, 29, 33–44.
- 1454 Garagnani, M., Wennekers, T., & Pulvermüller, F. (2008). A neuroanatomically
 1455 grounded Hebbian-learning model of attention-language interactions in the
 1456 human brain. *European Journal of Neuroscience*, 27(2), 492–513.
 1457 <http://doi.org/10.1111/j.1460-9568.2008.06015.x>
- 1458 Gerstner, W., Sprekeler, H., & Deco, G. (2012). Theory and simulation in
 1459 neuroscience. *Science (New York, N.Y.)*, 338(6103), 60–5.
 1460 <http://doi.org/10.1126/science.1227356>
- 1461 Hampshire, A., & Sharp, D. J. (2015). Contrasting network and modular
 1462 perspectives on inhibitory control. *Trends in Cognitive Sciences*, 19(8), 445–
 1463 52. <http://doi.org/10.1016/j.tics.2015.06.006>
- 1464 Haxby, J. V., Petit, L., Ungerleider, L. G., & Courtney, S. M. (2000). Distinguishing
 1465 the functional roles of multiple regions in distributed neural systems for
 1466 visual working memory. *NeuroImage*, 11(5 Pt 1), 380–91.
 1467 <http://doi.org/10.1006/nimg.2000.0592>
- 1468 Jirsa, V. K., & Haken, H. (1997). A derivation of a macroscopic field theory of the
 1469 brain from the quasi-microscopic neural dynamics. *Physica D: Nonlinear*
 1470 *Phenomena*, 99(4), 503–526. [http://doi.org/10.1016/S0167-2789\(96\)00166-2](http://doi.org/10.1016/S0167-2789(96)00166-2)
- 1471 Johnson Spencer, J. P., & Schöner, G., J. S. (2008). Moving to a higher ground:
 1472 the dynamic field theory and the dynamics of visual cognition. *New Ideas in*
 1473 *Psychology*, 26, 227–251.
- 1474 Johnson, J. S., Hollingworth, A., & Luck, S. J. (2008). The role of attention in the
 1475 maintenance of feature bindings in visual short-term memory. *Journal of*
 1476 *Experimental Psychology: Human Perception and Performance*, 34, 41–55.
- 1477 Johnson, J. S., Spencer, J. P., Luck, S. J., & Schöner, G. (2009). A dynamic
 1478 neural field model of visual working memory and change detection.
 1479 *Psychological Science*, 20, 568–577.
- 1480 Johnson, J. S., Spencer, J. P., Luck, S. J., & Schöner, G. (2009). A dynamic
 1481 neural field model of visual working memory and change detection.
 1482 *Psychological Science*, 20(5), 568–577. <http://doi.org/10.1111/j.1467-9280.2009.02329.x>
- 1484 Jonides, J., Schumacher, E. H., Smith, E. E., Koeppe, R. A., Awh, E., Reuter-
 1485 Lorenz, P. A., ... Willis, C. R. (1998). The role of parietal cortex in verbal

1486 working memory. *Journal of Neuroscience*, 18(13), 5026–5034.

1487 Kaladjian, a, Jeanningros, R., Azorin, J.-M., Anton, J.-L., & Mazzola-Pomietto, P.

1488 (2011). Impulsivity and neural correlates of response inhibition in

1489 schizophrenia. *Psychological Medicine*, 41(2), 291–299.

1490 <http://doi.org/10.1017/S0033291710000796>

1491 Kelso, J. A. S., Scholz, J. P., & Schoner, G. (1988). Dynamics governs switching

1492 among patterns of coordination in biological movement. *Physics Letters A*,

1493 134(1), 8–12. [http://doi.org/10.1016/0375-9601\(88\)90537-3](http://doi.org/10.1016/0375-9601(88)90537-3)

1494 Klaes, C., Schneegans, S., Schöner, G., & Gail, A. (2012). Sensorimotor

1495 Learning Biases Choice Behavior: A Learning Neural Field Model for

1496 Decision Making. *PLoS Comput Biol*, 8(11), e1002774.

1497 <http://doi.org/10.1371/journal.pcbi.1002774>

1498 Kopecz, K., & Schöner, G. (1995). Saccadic motor planning by integrating visual

1499 information and pre-information on neural, dynamic fields. *Biological*

1500 *Cybernetics*, 73, 49–69.

1501 Laing, C. R., & Chow, C. C. (2001). Stationary bumps in networks of spiking

1502 neurons. *Neural Computation*, 13(7), 1473–1494.

1503 <http://doi.org/10.1162/089976601750264974>

1504 Lipinski, J., Schneegans, S., Sandamirskaya, Y., Spencer, J. P., & Schöner, G.

1505 (2012). A neurobehavioral model of flexible spatial language behaviors.

1506 *Journal of Experimental Psychology. Learning, Memory, and Cognition*, 38,

1507 1490–1511. <http://doi.org/10.1037/a0022643>

1508 Lipinski, J., Spencer, J. P., & Samuelson, L. K. (2010). Corresponding delay-

1509 dependent biases in spatial language and spatial memory. *Psychological*

1510 *Research*, 74(3), 337–51. <http://doi.org/10.1007/s00426-009-0255-x>

1511 Logan, G. D., Yamaguchi, M., Schall, J. D., & Palmeri, T. J. (2015). Inhibitory

1512 control in mind and brain 2.0: Blocked-input models of saccadic

1513 countermanding. *Psychological Review*, 122(2), 115–147.

1514 <http://doi.org/10.1037/a0038893>

1515 Mack, M. L., Preston, A. R., & Love, B. C. (2013). Decoding the brain's algorithm

1516 for categorization from its neural implementation. *Current Biology*, 23(20),

1517 2023–2027. <http://doi.org/10.1016/j.cub.2013.08.035>

1518 Markounikau Igel, C., and Jancke, D., V. (2008). A Mesoscopic Model of VSD

1519 Dynamics Observed in Visual Cortex Induced by Flashed and Moving

1520 Stimuli. *Frontiers in Human Neuroscience. Conference Abstract: 10th*

1521 *International Conference on Cognitive Neuroscience*.

1522 Markounikau, V., Igel, C., Grinvald, A., & Jancke, D. (2010). A dynamic neural

1523 field model of mesoscopic cortical activity captured with voltage-sensitive

1524 dye imaging. *PLoS Computational Biology*, 6(9).

1525 <http://doi.org/10.1371/journal.pcbi.1000919>

1526 Markounikau, V., Igel, C., Grinvald, A., & Jancke, D. (2010). A dynamic neural

1527 field model of mesoscopic cortical activity captured with voltage-sensitive

1528 dye imaging. *PLoS Comput Biol*, 6(9).

1529 Markram, H., Muller, E., Ramaswamy, S., Reimann, M. W., Abdellah, M.,

1530 Sanchez, C. A., ... Schürmann, F. (2015). Reconstruction and Simulation of

1531 Neocortical Microcircuitry. *Cell*, 163(2), 456–492.

1532 <http://doi.org/10.1016/j.cell.2015.09.029>

1533 McDowell, K., Jeka, J. J., Schöner, G., & Hatfield, B. D. (1998). Testing dynamic
1534 field theory with directional arm movements. In *28th Annual Meeting of the*
1535 *Society for Neuroscience*. Los Angeles, CA.

1536 McDowell, K., Jeka, J. J., Schöner, G., & Hatfield, B. D. (2002). Behavioral and
1537 electrocortical evidence of an interaction between probability and task
1538 metrics in movement preparation. *Experimental Brain Research*, *144*, 303–
1539 313.

1540 Mechelli, A., Humphreys, G. W., Mayall, K., Olson, A., & Price, C. J. (2000).
1541 Differential effects of word length and visual contrast in the fusiform and
1542 lingual gyri during reading. *Proc Biol Sci*, *267*(1455), 1909–1913.
1543 <http://doi.org/10.1098/rspb.2000.1229>

1544 Monterosso, J. R., Aron, A. R., Cordova, X., Xu, J., & London, E. D. (2005).
1545 Deficits in response inhibition associated with chronic methamphetamine
1546 abuse. *Drug and Alcohol Dependence*, *79*(2), 273–7.
1547 <http://doi.org/10.1016/j.drugalcdep.2005.02.002>

1548 Munk, M. H. J., Linden, D. E. J., Muckli, L., Lanfermann, H., Zanella, F. E.,
1549 Singer, W., & Goebel, R. (2002). Distributed cortical systems in visual short-
1550 term memory revealed by event-related functional magnetic resonance
1551 imaging. *Cerebral Cortex (New York, N.Y. : 1991)*, *12*(8), 866–876.
1552 <http://doi.org/10.1093/cercor/12.8.866>

1553 Palmeri, T. J., Schall, J. D., & Logan, G. D. (2015). Neurocognitive Modeling of
1554 Perceptual Decision Making. In *The Oxford Handbook of Computational and*
1555 *Mathematical Psychology* (pp. 320–340).
1556 <http://doi.org/10.1093/oxfordhb/9780199957996.013.15>

1557 Perone, S., Simmering, V. R., & Spencer, J. P. (2011). Stronger neural dynamics
1558 capture changes in infants' visual working memory capacity over
1559 development. *Developmental Science*, *14*(6), 1379–92.
1560 <http://doi.org/10.1111/j.1467-7687.2011.01083.x>

1561 Perone, S., & Spencer, J. P. (2008). Establishing a link between infant looking
1562 and memory formation in a dynamic layered neural architecture. *Manuscript*
1563 *in Preparation*.

1564 Perone, S., & Spencer, J. P. (2013). Autonomous visual exploration creates
1565 developmental change in familiarity and novelty seeking behaviors. *Frontiers*
1566 *in Psychology*, *4*(September), 648. <http://doi.org/10.3389/fpsyg.2013.00648>

1567 Perone, S., & Spencer, J. P. (2013). Autonomy in Action: Linking the Act of
1568 Looking to Memory Formation in Infancy via Dynamic Neural Fields.
1569 *Cognitive Science*, *37*(1), 1–60. <http://doi.org/10.1111/cogs.12010>

1570 Perone, S., & Spencer, J. P. (2014). The co-development of looking dynamics
1571 and discrimination performance. *Developmental Psychology*, *50*(3), 837–52.
1572 <http://doi.org/10.1037/a0034137>

1573 Perone, S., Spencer, J. P., & Schöner, G. (2007). A dynamic field theory of visual
1574 recognition in infant looking tasks. In D. S. McNamara & J. G. Trafton (Eds.),
1575 *Proceedings of the Twenty-Ninth Annual Cognitive Science Society* (pp.
1576 1391–1396). Nashville, TN: Cognitive Science Society.

1577 Pessoa, L., Gutierrez, E., Bandettini, P., & Ungerleider, L. (2002). Neural

1578 correlates of visual working memory: fMRI amplitude predicts task
 1579 performance. *Neuron*, 35(5), 975–87. Retrieved from
 1580 <http://www.ncbi.nlm.nih.gov/pubmed/12372290>
 1581 Pessoa, L., & Ungerleider, L. G. (2004). Neural Correlates of Change Detection
 1582 and Change Blindness in a Working Memory Task — Cereb Cortex.
 1583 *Cerebral Cortex (New York, N.Y. : 1991)*, 14(5), 511–20.
 1584 <http://doi.org/10.1093/cercor/bhh013>
 1585 Pliszka, S. R., Liotti, M., & Woldorff, M. G. (2000). Inhibitory control in children
 1586 with attention-deficit/hyperactivity disorder: Event-related potentials identify
 1587 the processing component and timing of an impaired right-frontal response-
 1588 inhibition mechanism. *Biological Psychiatry*, 48(3), 238–246.
 1589 [http://doi.org/10.1016/S0006-3223\(00\)00890-8](http://doi.org/10.1016/S0006-3223(00)00890-8)
 1590 Rescorla, R. A., & Wagner, A. R. (1972). *A theory of Pavlovian conditioning:*
 1591 *Variations in the effectiveness of reinforcement and nonreinforcement.* (In A.
 1592 H. B).
 1593 Sala, J. B., & Courtney, S. M. (2007). Binding of what and where during working
 1594 memory maintenance. *Cortex; a Journal Devoted to the Study of the*
 1595 *Nervous System and Behavior*, 43(1), 5–21. [http://doi.org/10.1016/S0010-](http://doi.org/10.1016/S0010-9452(08)70442-8)
 1596 [9452\(08\)70442-8](http://doi.org/10.1016/S0010-9452(08)70442-8)
 1597 Sala, J. B., Rämä, P., & Courtney, S. M. (2003). Functional topography of a
 1598 distributed neural system for spatial and nonspatial information maintenance
 1599 in working memory. *Neuropsychologia*, 41(3), 341–356.
 1600 [http://doi.org/10.1016/S0028-3932\(02\)00166-5](http://doi.org/10.1016/S0028-3932(02)00166-5)
 1601 Sala-Llonch, R., Peña-Gómez, C., Arenaza-Urquijo, E. M., Vidal-Piñeiro, D.,
 1602 Bargalló, N., Junqué, C., & Bartrés-Faz, D. (2012). Brain connectivity during
 1603 resting state and subsequent working memory task predicts behavioural
 1604 performance. *Cortex*, 48(9), 1187–1196.
 1605 <http://doi.org/10.1016/j.cortex.2011.07.006>
 1606 Samuelson, L. K., Jenkins, G. W., & Spencer, J. P. (2015). Grounding cognitive-
 1607 level processes in behavior: The view from dynamic systems theory. *Topics*
 1608 *in Cognitive Science*, 7(2), 191–205. <http://doi.org/10.1111/tops.12129>
 1609 Sandamirskaya, Y., & Schöner, G. (2008). Dynamic field theory of sequential
 1610 action: a model and its implementation on an embodied agent. *Proceedings*
 1611 *of the International Conference on Development and Learning.*
 1612 Sandamirskaya, Y., & Schöner, G. (2010). An embodied account of serial order:
 1613 how instabilities drive sequence generation. *Neural Networks : The Official*
 1614 *Journal of the International Neural Network Society*, 23(10), 1164–79.
 1615 <http://doi.org/10.1016/j.neunet.2010.07.012>
 1616 Sandamirskaya, Y., Zibner, S. K. U., Schneegans, S., & Schöner, G. (2013).
 1617 Using Dynamic Field Theory to extend the embodiment stance toward higher
 1618 cognition. *New Ideas in Psychology*, 31(3), 322–339.
 1619 <http://doi.org/10.1016/j.newideapsych.2013.01.002>
 1620 Schneegans, S., & Schöner, G. (2012). A neural mechanism for coordinate
 1621 transformation predicts pre-saccadic remapping. *Biological Cybernetics*,
 1622 106(2), 89–109. <http://doi.org/10.1007/s00422-012-0484-8>
 1623 Schneegans, S., Spencer, J. P., Schöner, G., Hwang, S., & Hollingworth, A.

1624 (2014). Dynamic interactions between visual working memory and saccade
1625 target selection. *Journal of Vision*, 14(11)(9), 1–23.
1626 <http://doi.org/10.1167/14.11.9>

1627 Schöner, G., & Kelso, J. A. S. (1988). Dynamic pattern generation in behavioral
1628 and neural systems. *Science*, 239, 1513–1520.

1629 Schöner, G., Spencer, J. P., & The DFT Research Group. (2015). *Dynamic*
1630 *Thinking: A Primer on Dynamic Field Theory*. New York, NY: Oxford
1631 University Press.

1632 Schutte, A. R., & Spencer, J. P. (2002). Generalizing the dynamic field theory of
1633 the A-not-B error beyond infancy: Three-year-olds' delay- and experience-
1634 dependent location memory biases. *Child Development*, 73, 377–404.

1635 Schutte, A. R., & Spencer, J. P. (2007). Planning “discrete” movements using a
1636 continuous system: Insights from a dynamic field theory of movement
1637 preparation. *Motor Control*, 11, 166–208.

1638 Schutte, A. R., Spencer, J. P., & Schöner, G. (2003). Testing the dynamic field
1639 theory: Working memory for locations becomes more spatially precise over
1640 development. *Child Development*, 74(5), 1393–1417.

1641 Simmering, V. R. (n.d.). Working memory capacity in context: Modeling dynamic
1642 processes of behavior, memory, and development. *Monographs of the*
1643 *Society for Research in Child Development*.

1644 Simmering, V. R., Peterson, C., Darling, W. G., & Spencer, J. P. (2008). Location
1645 memory biases reveal the challenges of coordinating visual and kinesthetic
1646 reference frames. *Experimental Brain Research*, 184, 165–178.

1647 Simmering, V. R., & Spencer, J. P. (2007). Creating and destroying frames of
1648 reference for spatial working memory. *Manuscript in Preparation*.

1649 Smith, L. B., Thelen, E., Titzer, R., & McLin, D. (1999). Knowing in the context of
1650 acting: The task dynamics of the A-not-B error. *Psychological Review*, 106,
1651 235–260.

1652 Smith, S. M., Fox, P. T., Miller, K. L., Glahn, D. C., Fox, P. M., Mackay, C. E., ...
1653 Beckmann, C. F. (2009). Correspondence of the brain's functional
1654 architecture during activation and rest. *Proceedings of the National Academy*
1655 *of Sciences of the United States of America*, 106(31), 13040–5.
1656 <http://doi.org/10.1073/pnas.0905267106>

1657 Spencer, J. P., & Schöner, G. (2003). Bridging the representational gap in the
1658 dynamic systems approach to development. *Developmental Science*, 6(4),
1659 392–412. <http://doi.org/10.1111/1467-7687.00295>

1660 Thelen, E., Schöner, G., Scheier, C., & Smith, L. B. (2001). The dynamics of
1661 embodiment: A field theory of infant perseverative reaching. *Behavioral &*
1662 *Brain Sciences*, 24, 1–86.

1663 Turner, B. M., Forstmann, B. U., Love, B. C., Palmeri, T. J., & Van Maanen, L.
1664 (2016). Approaches to analysis in model-based cognitive neuroscience.
1665 *Journal of Mathematical Psychology*.
1666 <http://doi.org/10.1016/j.jmp.2016.01.001>

1667 Turvey MT, S. R. (1995). *Toward an ecological physics and a physical*
1668 *psychology*. (M. D. Solso R, Ed.) *The Science of the Mind: 2001 and beyond*.
1669 Oxford University Press; Oxford.

1670 Usher, M., & McClelland, J. L. (2001). The time course of perceptual choice: the
1671 leaky, competing accumulator model. *Psychological Review*.
1672 <http://doi.org/10.1037/0033-295X.108.3.550>
1673 Wiecki, T. V., & Frank, M. J. (2013). A computational model of inhibitory control in
1674 frontal cortex and basal ganglia. *Psychological Review*, *120*(2), 329–355.
1675 <http://doi.org/10.1037/a0031542>
1676 Wijeakumar, S., Magnotta, V. A., Buss, A. T., Ambrose, J. P., Wifall, T. A.,
1677 Hazeltine, E., & Spencer, J. P. (2015). Response control networks are
1678 selectively modulated by attention to rare events and memory load
1679 regardless of the need for inhibition. *NeuroImage*, *120*, 331–344.
1680 <http://doi.org/10.1016/j.neuroimage.2015.07.026>
1681 Wilson, H. R., & Cowan, J. D. (1973). A mathematical theory of the functional
1682 dynamics of cortical and thalamic nervous tissue. *Kybernetik*, *13*, 55–80.
1683 Wong, K. F., & Wang, X. J. (2006). A recurrent network mechanism of time
1684 integration in perceptual decisions. *J Neurosci*, *26*(4), 1314–1328.
1685 <http://doi.org/10.1523/JNEUROSCI.3733-05.2006>
1686

1687 **Appendix A**

1688 A.1. Dynamic Field (DNF) Model for Go/Nogo Paradigm

1689 The dynamic field (DNF) model for the Go/Nogo paradigm consists of 7
1690 coupled neuronal sub-networks as illustrated in Figure 2: the visual field (vis);
1691 spatial attention field (sAtn); feature attention (fAtn); contrast field (con); working
1692 memory (wm); and the “decision system” consisting of two nodes (go and Nogo).
1693 The DNF Model 1 is therefore defined by a system of five integral-differential
1694 equations (A.1) – (A.5) and two ordinary differential equations (A.6) – (A.7), as
1695 listed below.

1696 Each equation is described by a sum of several components. The first three
1697 terms correspond to the local field interactions, while local noise is modeled by the
1698 function η . All terms that depend on two distinct indices are associated with long-
1699 range, inter-field coupling. Applied stimulus, when appropriate, is given by function
1700 s . Excitatory coupling takes positive values, while inhibitory coupling is negative.
1701 The functional topography assumes local excitation and lateral inhibition, and it is
1702 modeled by a difference of two Gaussians resulting in a Mexican-hat connectivity.
1703 The dot in \dot{u} represents the derivative of neuronal activity u with respect to time t .
1704 Detailed definitions of each coupling term are included in Sections A.2–A.4, and
1705 the set of parameters used in the simulation of this DNF model are listed in Tables
1706 A.2.1, A.3.1 and A.4.1.

1707 We start by describing the equation for the visual field. Besides local
1708 neuronal population interactions, the visual field receives excitatory connections
1709 from the spatial attention and the feature attention fields via convolutions $c_{vis,sAtn} * g_{sAtn}(u_{sAtn})$
1710 and $c_{vis,fAtn} * g_{fAtn}(u_{fAtn})$. It is also subject to external stimulus
1711 $s_{vis}(x, y)$.

$$\begin{aligned} 1712 \quad \tau_e \dot{u}_{vis}(x, y, t) = & -u_{vis}(x, y, t) + h_{vis} + \iint c_{vis}(x - x', y - y') g_{vis}(u_{vis}(x', y', t)) dx' dy' \\ 1713 \quad & + \int c_{vis,sAtn}(x - x') g_{sAtn}(u_{sAtn}(x', t)) dx' \\ 1714 \quad & + \int c_{vis,fAtn}(y - y') g_{fAtn}(u_{fAtn}(y', t)) dy' + \eta_{vis}(x, y, t) + s_{vis}(x, y) \\ 1715 \end{aligned} \tag{A.1}$$

1716 The spatial attention field receives two excitatory inputs: projections
 1717 $c_{sAtn,vis} * g_{sAtn}(u_{vis})$ from the visual field, and a sub-threshold bump activity
 1718 $s_{sAtn}(x)$. The latter is centered at the position of stimulus presentation and it
 1719 simulates the response of the network during the fixation stage of the task.

$$\begin{aligned}
 1720 \quad \tau_e \dot{u}_{sAtn}(x, t) = & -u_{sAtn}(x, t) + h_{sAtn} + \int c_{sAtn}(x - x') g_{sAtn}(u_{sAtn}(x', t)) dx' \\
 1721 \quad & + \iint c_{sAtn,vis}(x - x') g_{vis}(u_{vis}(x', y', t)) dy' dx' + \eta_{sAtn}(x, t) + s_{sAtn}(x) \\
 1722 \quad & \hspace{15em} (A.2)
 \end{aligned}$$

1723 The feature attention field receives excitatory inputs from the visual,
 1724 contrast and working memory fields:

$$\begin{aligned}
 1725 \quad \tau_e \dot{u}_{fAtn}(y, t) = & -u_{fAtn}(y, t) + h_{fAtn} + \int c_{fAtn}(y - y') g_{fAtn}(u_{fAtn}(y', t)) dy' \\
 1726 \quad & + \iint c_{fAtn,vis}(y - y') g_{vis}(u_{vis}(x', y', t)) dy' dx' \\
 1727 \quad & + \int c_{fAtn,con}(y - y') g_{con}(u_{con}(y', t)) dy' + \int c_{fAtn,wm}(y - y') g_{wm}(u_{wm}(y', t)) dy' \\
 1728 \quad & + \eta_{fAtn}(y, t) \\
 1729 \quad & \hspace{15em} (A.3)
 \end{aligned}$$

1730 The contrast field receives feedforward excitatory connections from the
 1731 visual and feature attention fields; inhibitory connections from the working memory
 1732 field; and excitatory feedback from the nogo node. To account for learning during
 1733 the pre-task instruction step, a sub-threshold input $s_{con}(y)$ with activity bumps
 1734 localized at the Nogo colors is also included.

$$\begin{aligned}
 1735 \quad \tau_e \dot{u}_{con}(y, t) = & -u_{con}(y, t) + h_{con} + \int c_{con}(y - y') g_{con}(u_{con}(y', t)) dy' \\
 1736 \quad & + \iint c_{con,vis}(y - y') g_{vis}(u_{vis}(x', y', t)) dy' dx' + \int c_{con,fAtn}(y - y') g_{fAtn}(u_{fAtn}(y', t)) dy' \\
 1737 \quad & + \int c_{con,wm}(y - y') g_{wm}(u_{wm}(y', t)) dy' \\
 1738 \quad & + a_{con,nogo} \times g_{nogo}(u_{nogo}(t)) + \eta_{con}(y, t) + s_{con}(y) \quad (A.4)
 \end{aligned}$$

1739 Similarly, the working memory field receives feed-forward excitatory
 1740 connections from the visual and feature attention fields; inhibitory connections from
 1741 the contrast field; and excitatory feedback from the go node. In addition, we include
 1742 a sub-threshold input $s_{wm}(y)$ of activity bumps localized at the Go colors which
 1743 simulates learning during the pre-task instruction step,

1744 $\tau_e \dot{u}_{wm}(y, t) = -u_{wm}(y, t) + h_{wm} + \int c_{wm}(y - y') g_{wm}(u_{wm}(y', t)) dy'$
1745 $+ \iint c_{wm,vis}(y - y') g_{vis}(u_{vis}(x', y', t)) dy' dx'$
1746 $+ \int c_{wm,fAtn}(y - y') g_{fAtn}(u_{fAtn}(y', t)) dy'$
1747 $+ \int c_{wm,con}(y - y') g_{con}(u_{con}(y', t)) dy' + a_{wm,go} \times g_{go}(u_{go}(t)) + \eta_{wm}(y, t)$
1748 $+ s_{wm}(y)$
1749 (A.5)

1750 The go and nogo nodes are coupled by mutual inhibition. In addition, feed-
1751 forward excitation is projected from the working memory field to the go node, and
1752 from the contrast field to the nogo node respectively.

1753 $\tau_e \dot{u}_{go}(t) = -u_{go}(t) + h_{go} + a_{go} \times g_{go}(u_{go}(t))$
1754 $+ a_{go,nogo} \times g_{nogo}(u_{nogo}(t)) + a_{go,wm} \times \int g_{wm}(u_{wm}(y', t)) dy' + \eta_{go}(t)$
1755 (A.6)

1756 $\tau_e \dot{u}_{nogo}(t) = -u_{nogo}(t) + h_{nogo} + a_{nogo} \times g_{nogo}(u_{nogo}(t))$
1757 $+ a_{nogo,go} \times g_{go}(u_{go}(t)) + a_{nogo,con} \times \int g_{con}(u_{con}(y', t)) dy' + \eta_{nogo}(t)$
1758 (A.7)

1759 A.2. Local Field Interactions

1760 All parameters associated with local interactions in the DNF model above
1761 are listed in Table A.2.1.

1762 The Gaussian interaction kernel that determines the spread of activation
1763 inside a given field to neighboring units (see parameters $\sigma_{j,E}$ and $\sigma_{j,I}$ in Table
1764 A.2.1) with strengths determined by the amplitude parameters $a_{j,E}$, $a_{j,I}$ and
1765 $a_{j,global}$ is defined by

1766 $c_j(z - z') = a_{j,E} \text{Exp} \left[-\frac{(z - z')^2}{2\sigma_{j,E}^2} \right] - a_{j,I} \text{Exp} \left[-\frac{(z - z')^2}{2\sigma_{j,I}^2} \right] + a_{j,global}$
1767 (A.8)

1768 Here the variable $z = x$ or $z = y$ spans either the spatial dimension ($x \in S$) or the
1769 feature (color) dimension ($y \in F$), while the index $j \in \{sAtn, fAtn, con, wm\}$
1770 corresponds to the neural field spatial attention, feature attention, contrast field or

1771 working memory, respectively. The gain output function g normalizes the field
 1772 activation, and is assumed to be the sigmoidal

$$1773 \quad g(u) = \frac{1}{1 + \text{Exp}[-\beta u]} \quad (\text{A.9})$$

1774 with threshold set to zero and steepness parameter β . Consequently, activation
 1775 levels lower than the threshold contribute relatively little to neural interactions,
 1776 while positive activation levels (higher than the threshold 0) contribute strongly to
 1777 neural interactions.

1778 Each neural network is subject to spatially correlated noise $\eta_j(z, t)$ defined
 1779 as the convolution between a Gaussian kernel and white noise $\xi(z, t)$

$$1780 \quad \eta_j(z, t) = \int a_{j,noise} \text{Exp} \left[-\frac{(z-z')^2}{2\sigma_{j,noise}^2} \right] \xi(z', t) dz'. \quad (\text{A.10})$$

1781 Note that the variable $\xi(z, t)$ takes random values from a normal distribution with
 1782 zero mean and unit standard deviation $\mathcal{N}(0,1)$ but has its strength scaled with
 1783 $1/\sqrt{dt}$.

1784 Similar definitions are given for the visual field ($j = vis$) which spans two
 1785 coordinates, the spatial and color representations. In this case, the convolution
 1786 $c_{vis} * g_{vis}(u_{vis})$ and the noise η_{vis} are two-dimensional functions so the Gaussian
 1787 interaction kernel and the spatially correlated noise are defined by

$$1788 \quad c_j(x - x', y - y') \\
 1789 \quad = a_{j,E} \text{Exp} \left[-\frac{(x - x')^2}{2\sigma_{j,E}^2} \right] \text{Exp} \left[-\frac{(y - y')^2}{2\sigma_{j,E}^2} \right] \\
 1790 \quad + a_{j,I} \text{Exp} \left[-\frac{(x - x')^2}{2\sigma_{j,I}^2} \right] \text{Exp} \left[-\frac{(y - y')^2}{2\sigma_{j,I}^2} \right] + a_{j,global} \\
 1791 \quad (\text{A.11})$$

1792 and

$$1793 \quad \eta_j(x, y, t) = \iint a_{j,noise} \text{Exp} \left[-\frac{(x - x')^2}{2\sigma_{j,noise}^2} \right] \text{Exp} \left[-\frac{(y - y')^2}{2\sigma_{j,noise}^2} \right] \xi(x', y', t) dx' dy' \\
 1794 \quad (\text{A.12}) \\
 1795$$

1796 On the other hand, the go and nogo nodes with index $j \in \{go, nogo\}$ are assumed
 1797 to have global connectivity. Then their local field interactions are simply the product

1798
$$a_j \times g_j(u_j(t)) \tag{A.13}$$

1799 between the gain function and constant a_j . The noise function is defined by

1800
$$\eta_j(t) = a_{j,noise} \times \xi(t) \tag{A.14}$$

1801

1802 A.3. Long Range (Inter-Network) Coupling

1803 The coupling between two distinct fields of the neural network is defined by
 1804 a Gaussian kernel as well. Thus, if field k receives input from field j then the
 1805 connectivity function is the convolution $c_{k,j}(\cdot) * g_j(u_j(\cdot, t))$ with kernel

1806
$$c_{k,j}(z - z') = a_{k,j} \text{Exp} \left[-\frac{(z - z')^2}{2\sigma_{k,j}^2} \right]$$

 1807 (A.15)

1808 In particular, if the coupling is a projection of the visual field ($j = vis$) into either of
 1809 the fields spatial attention, feature attention, contrast or working memory (k), then
 1810 the convolution is a double-integral over the two-dimensional set, $S \times F$. The
 1811 Gaussian kernel depends, however, only on one variable (for example, x) so the
 1812 integration over the other variable (y) ultimately reduces to a summation of the
 1813 output gain along the secondary dimension y .

1814 If the coupling is a projection of the working memory (or contrast field) into
 1815 the *go* (or *nogo node*), then the kernel of the convolution function reduces to a
 1816 constant,

1817
$$c_{k,j} = a_{k,j} \tag{A.16}$$

 1818

1819 In addition, if the coupling is between the *go* and *nogo* nodes then the convolution
 1820 is simply the product $c_{k,j} \times g_j(u_j(t))$ and, again, $c_{k,j} = a_{k,j}$.

1821 Table A.3.1 summarizes all parameter values associated with long range
 1822 coupling in the DNF model.

1823 A.4. Stimulus Functions

1824 All parameters associated with stimuli in the DNF model appear in Table
 1825 A.4.1. Stimuli s_j to field j are modeled by normalized Gaussian inputs centered at
 1826 particular position $z_{j,s}$ in the neural field, and with spread parameter $\sigma_{j,s}$ and

1827 amplitude $a_{j,s}$. In particular, stimuli applied to the spatial attention, contrast and
 1828 working memory fields induce local sub-threshold bump(s) of activity in the
 1829 absence of the external stimulus $s_{vis}(x, y)$.

$$1830 \quad s_{vis}(x, y) = a_{vis,s} \times \frac{1}{2\pi \sigma_{vis,s}^2} \text{Exp} \left[-\frac{(x - x_{vis,s})^2}{2\sigma_{vis,s}^2} \right] \text{Exp} \left[-\frac{(y - y_{vis,s})^2}{2\sigma_{vis,s}^2} \right]$$

1831

$$1832 \quad s_{sAtn}(x) = a_{sAtn,s} \times \frac{1}{\sqrt{2\pi} \sigma_{sAtn,s}} \text{Exp} \left[-\frac{(x - x_{sAtn,s})^2}{2\sigma_{sAtn,s}^2} \right]$$

1833

$$1834 \quad s_{con}(y) = a_{con,s} \times \frac{1}{\sqrt{2\pi} \sigma_{con,s}} \sum_{l=1}^{load/2} \text{Exp} \left[-\frac{(y - y_{con,s}^l)^2}{2\sigma_{con,s}^2} \right]$$

1835

$$1836 \quad s_{wm}(y) = a_{wm,s} \times \frac{1}{\sqrt{2\pi} \sigma_{wm,s}} \sum_{l=1}^{load/2} \text{Exp} \left[-\frac{(y - y_{wm,s}^l)^2}{2\sigma_{wm,s}^2} \right]$$

1837

(A.17)

1838 The sub-threshold activity bump in the spatial attention field is assumed to form
 1839 during the fixation stage and prior to application of the Go/Nogo stimulus $s_{vis}(x, y)$.
 1840 Similarly, sub-threshold activity bumps in the contrast and working memory fields
 1841 are assumed to form during the instruction stage when the subject learns the Go
 1842 and Nogo colors, and again prior to application of the external stimulus $s_{vis}(x, y)$.
 1843 For example, Load 4 requires learning of two Go colors and other two Nogo colors.
 1844 Therefore, during the numerical simulation time, two sub-threshold activity bumps
 1845 centered at the Go colors are placed in the working memory field, and two sub-
 1846 threshold activity bumps centered at the Nogo colors are placed in the contrast
 1847 field.

1848 Table A.2.1. Local field interactions: parameter values used in the simulation of the
1849 DNF model. See also Eqs. (A.1)–(A.5) and (A.8)–(A.14). Differences in parameter
1850 values between **Model 2 (shown in the table)** and Model 1 are highlighted in red
1851 and should be read as follows: Model 1 does not include any “condition of
1852 satisfaction” so, for it, last column in the table should be ignored. In addition, in
1853 Model 1, the amplitude a_j of all-to-all coupling for go and nogo nodes is fixed to
1854 $a_{Go} = 1$ and $a_{NoGo} = 3$ (see columns 8 and 9 in the table).

Symbol	Meaning	Parameter values for particular neural field j							
		Visual Field $j = vis$	Spatial Attention $j = sAtn$	Feature Attention $j = fAtn$	Contrast Field $j = con$	Working Memory $j = wm$	Go $j = go$	NoGo $j = nogo$	Cond. of Satis. $j = CoS$
τ_e	Timescale	20	20	20	20	20	20	20	20
h_j	Neuronal resting level	-5	-5	-5	-5	-5	-5	-5	-5
$a_{j,E}$	Amplitude of lateral excitation	0.44	0.64	0.80	1.20	1.20			
$a_{j,I}$	Amplitude of lateral inhibition	-0.12	0	0	-0.32	-0.32			
$\sigma_{j,E}$	Spread of lateral excitation	5	5	5	5	5			
$\sigma_{j,I}$	Spread of lateral inhibition	10	10	10	10	10			
$\alpha_{j,global}$	Amplitude of global inhibition	-0.002	-1	-1	0	0			
a_j	Amplitude all-to-all coupling						2, 1 or 3*	2, 3 or 1*	2
β_j	Steepness of the gain function	2	2	4	2	2	1	1	1
$\alpha_{j,noise}$	Amplitude of correlated noise	0.40	0.40	1.60	1.60	1.60	1	1	
$\sigma_{j,noise}$	Spread of noise	1	1	1	1	1			
$x, x' \in S$	Field size for spatial dimension S	101	101						
$y, y' \in F$	Field size for feature (color) dimension F	204		204	204	204			

* First value in Load 2/4/6, Second value in Prop 25, Third value in Prop 75 (Model 2)

1855
1856
1857
1858

1859 Table A.3.1. Long range (inter-network) coupling: parameter values used in the
1860 simulation of the DNF model. For all existing connections j to k where it makes
1861 sense, the spread of activation takes the value $\sigma_{k,j} = 5$. See also Eqs. (A.6)–(A.7)
1862 and (A.15)–(A.16). Differences in parameter values between **Model 2 (shown in
1863 the table)** and Model 1 are highlighted in red and should be read as follows: Model

1864 1 does not include any “condition of satisfaction” so, for it, last row and last column
 1865 in the table should be ignored. In addition, in Model 1, the bi-directional coupling
 1866 between *wm* and *con* is $a_{con,wm} = a_{wm,con} = -0.56$ and the bi-directional coupling
 1867 between *con* and *Nogo* is $a_{con,nogo} = a_{nogo,con} = 1$.

Symbol / Meaning		Neural Fields	Input layer <i>j</i>								
			<i>vis</i>	<i>sAtn</i>	<i>fAtn</i>	<i>con</i>	<i>wm</i>	<i>go</i>	<i>nogo</i>	<i>CoS</i>	
$a_{k,j}$	Amplitude of the coupling from field <i>j</i> into field <i>k</i>	Output Layer <i>k</i>	<i>vis</i>		0.24	0.08					
			<i>sAtn</i>	0.16							
			<i>fAtn</i>	0.32			0.16	0.16			
			<i>con</i>	0.16		0.16		-0.60		0.27	-10
			<i>wm</i>	0.16		0.16	-0.60		0.27		-10
			<i>go</i>					0.28		-6	
			<i>nogo</i>				0.28		-6		
			<i>CoS</i>						4	4	

*Width/spread of all field → field connections is 5, except inhibitory *wm* ↔ *con* connections have width 60.

1868

1869 Table A.4.1. Stimulus functions: parameter values used in the simulation of the
 1870 DNF model. See also Eqs. (A.1), (A.2), (A.4), (A.5) and (A.17).

Condition	Neural Field j	Stimulus strength $a_{j,s}$	Spread of stimulation $\sigma_{j,s}$	Spatial coordinate(s) at the center of stimulus $x_{j,s}$	Feature (color) coordinate(s) at the center of stimulus $y_{j,s}$
Load 2	vis	5.4	3	51	Either of 18 or 52
	sAtn	3	3	51	
	con	1.97	3		52
	wm	1.97	3		18
Load 4	vis	5.4	3	51	Either of 18, 52, 86 or 120
	sAtn	3	3	51	
	con	1.87	3		52 and 120
	wm	1.87	3		18 and 86
Load 6	vis	5.4	3	51	Either of 18, 52, 86, 120, 154 or 188
	sAtn	3	3	51	
	con	1.78	3		52 and 120 and 188
	wm	1.78	3		18 and 86 and 154
Load 4 proportion 25/75 Go/NoGo	vis	5.4	3	51	Either of 18, 52, 86 or 120
	sAtn	3	3	51	
	con	1.90	3		52 and 120
	wm	1.84	3		18 and 86
Load 4 proportion 75/25 Go/NoGo	vis	5.4	3	51	Either of 18, 52, 86 or 120
	sAtn	3	3	51	
	con	1.84	3		52 and 120
	wm	1.90	3		18 and 86

1871